Acta Materialia 290 (2025) 120921



Contents lists available at ScienceDirect

Acta Materialia

journal homepage: www.elsevier.com/locate/actamat



Full length article

Effective transport and mechanical properties of two-phase materials across the order-disorder spectrum

M. Skolnick [a], S. Torquato [a,b,c,d,*]

[a] Department of Chemistry, Princeton University, Princeton, NJ, 08544, USA
[b] Department of Physics, Princeton University, Princeton, NJ, 08544, USA
[c] Princeton Institute of Materials, Princeton University, Princeton, NJ, 08544, USA
[d] Program in Applied and Computational Mathematics, Princeton University, Princeton, NJ, 08544, USA

ARTICLE INFO

Keywords:
Hyperuniformity
Effective properties
Heterogeneous materials
Strong contrast expansions

ABSTRACT

Two-phase heterogeneous materials arise in a plethora of natural and synthetic situations, such as alloys, composites, geological media, complex fluids, and biological media, exhibit a wide-variety of microstructures, and thus display a broad-spectrum of effective physical properties. Elucidating how microstructural details (e.g., specific surface, phase volume fractions, and phase geometries and topologies) influence two-phase materials' effective transport and mechanical properties enhances our fundamental understanding of microstructure–property relationships, and is of great practical use in the design of structural and functional materials. Here, we compute the three-point microstructural parameters ζ_2 and η_2 for phase 2 to evaluate bounds and accurate approximation formulas on the effective thermal/electrical conductivities σ_e as well as the bulk K_e and shear G_e moduli of a wide class of disordered 2D and 3D material microstructures; including various dispersions of hard and penetrable particles, certain amorphous dispersions, and networks. These parameters are determined using a Monte Carlo integration scheme that incorporates certain algorithmic enhancements that improve upon the accuracy and performance of previous methods. Our results reveal that ζ_2 and η_2 are generally sensitive to the phase-connectedness properties of the diverse set of microstructures we consider here. Using numerical simulations and rigorous approximations that incorporate ζ_2 and η_2, we show that certain disordered microstructures nearly realize the Hashin–Shtrikman lower and upper bounds on σ_e, K_e, and G_e across volume fractions. We also describe how our algorithm can be used in inverse methodologies to realize ordered and disordered materials with desirable effective physical properties by targeting specific values of ζ_2 and η_2, and hence aid in materials by design.

1. Introduction

Two-phase heterogeneous materials abound in natural and synthetic systems; examples include composites, porous media, polymer blends, colloids, complex fluids, cellular solids, geological media, and biological media [1–8]. The microstructures of such materials exhibit a diverse set of possible phase geometries and topologies, as well as varying degrees of order and disorder across length scales [9]. A glimpse of such microstructural diversity is illustrated by the examples depicted in Fig. 1, including a stealthy hyperuniform disk packing [10,11], dispersions of fully penetrable disks and ellipses [1], a garden-variety disordered amorphous microstructure [12–15], a packing of thin rectangular platelets, and a thickened network derived from a stealthy hyperuniform point pattern [16]. Given that a material's effective transport and mechanical properties depend in a nontrivial manner on its microstructure and phase constituents [1–3,17–21], the aforementioned microstructural variety gives rise to a broad-spectrum of potential effective material properties.

In particular, it is well-known that the effective properties of heterogeneous materials generally depend on an *infinite-set* of correlation functions that fully characterize the microstructure [1,18,20,22,23]. Since such information is typically not available, it is useful to devise estimates of the effective properties that depend on a limited set of nontrivial microstructural information [1,3]. For example, the three-point microstructural parameters ζ_p and η_p, which incorporate such information via functionals of the one-, two-, and three-point correlation functions of phase p (=1 or 2) (see Sections 2.1 and 2.3 for definitions), provide a powerful route to accurately estimate and rigorously bound the effective physical properties of a structurally diverse set of ordered and disordered material microstructures [23–28].

* Corresponding author at: Department of Chemistry, Princeton University, Princeton, NJ, 08544, USA.
E-mail address: torquato@electron.princeton.edu (S. Torquato).

https://doi.org/10.1016/j.actamat.2025.120921
Received 17 December 2024; Received in revised form 7 March 2025; Accepted 8 March 2025
Available online 19 March 2025
1359-6454/© 2025 Acta Materialia Inc. Published by Elsevier Inc. All rights are reserved, including those for text and data mining, AI training, and similar technologies.

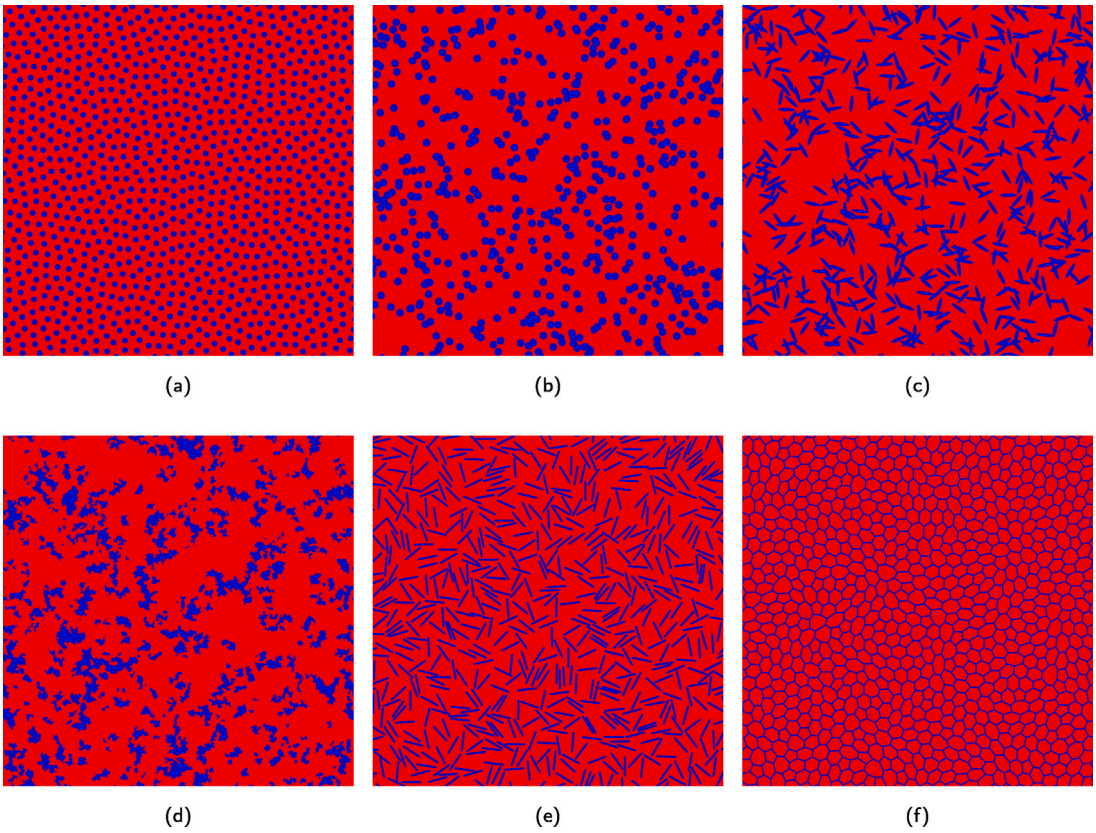


Fig. 1. Two-dimensional model systems that illustrate the diversity of possible material microstructures: (a) a special $\chi = 0.45$ stealthy hyperuniform hard disk packing [10,11], dispersions of fully penetrable (b) disks and (c) ellipses [1], (d) a garden-variety disordered amorphous microstructure [12–15], (e) a packing of thin, rectangular platelets, and (f) a disordered thickened network derived from a $\chi = 0.48$ stealthy hyperuniform point pattern [16]. These six microstructures as well as their 3D analogues are among the set of models that we consider in this paper and are described in Section 3. In these images, phase 1 is colored red and phase 2 is colored blue. For all microstructures shown, the phase 2 volume fraction is $\phi_2 = 0.20$.

To enhance our basic understanding of microstructure–property relationships and inform the design of structural and functional materials, we examine how and to what extent specific microstructural qualities influence a material's effective conductive and mechanical properties in this paper. We accomplish this task by computing the three-point microstructural parameters ζ_p and η_p for a comprehensive set of 2D and 3D model material microstructures with a wide spectrum of unique phase geometries, phase topologies, and inversion symmetry properties (see Section 2 for definitions), as well as hyperuniform and nonhyperuniform volume fraction fluctuations. By examining different model microstructures across dimensions, we also investigate the effect of dimensionality on these microstructure–property relationships.

Despite the distinct microstructural characteristics of the model systems that we consider, we can accurately estimate their effective physical properties by utilizing various approximations in which the three-point parameters ζ_p and η_p arise. Specifically, the parameter ζ_p appears in different approximations of the effective conductivity of materials whose microstructures consist of certain dispersions [1,28], possess phase-inversion symmetry [1], and exhibit phase bicontinuity[1] [29], as well as in approximations of the effective bulk modulus and, along with the parameter η_p, the effective shear modulus of certain dispersions [23,30,31]. The parameter ζ_p also arises in an accurate approximation of the fluid permeability for certain porous materials [29,32,33]. By applying to specific classes of microstructures (i.e., dispersions, phase-inversion symmetric, bicontinuous) the aforementioned approximations accurately capture the large range of distinct effective physical properties displayed by these systems. Moreover, the parameters ζ_p and η_p determine rigorous three-point microstructural bounds on the effective conductivity, bulk modulus, and shear modulus [24,25,27,28,34–42]. By incorporating up to three-point microstructural information, the aforementioned bounds improve upon the well-known Hashin–Shtrikman bounds [43–46]. Specific mathematical details on ζ_p, η_p, and the aforementioned approximations and bounds are provided in Section 2.3.

The microstructural parameters ζ_p and η_p have been computed for various periodic microstructures, including disks [47–49], spheres [47], and superballs [50] arranged on lattices, as well as arrays of triangle-, hexagon- [51] and superdisk- [52] shaped inclusions. The parameters ζ_p and η_p have also been ascertained to estimate the effective conductive and linear elastic properties for certain *disordered* model material microstructures, including monodisperse fully penetrable disks [53,54], spheres [55–57], hollow spheres [58], ellipsoids [57] as well as monodisperse and polydisperse equilibrium non-overlapping disks [59–62] and spheres [63–66]. The three-point parameters for symmetric-cell materials [67] have been obtained as functions of phase composition for circular [27,68], spherical [27,67], ellipsoidal [1], cubical [69], as well as triangular, square, and hexagonal [1,70] cell geometries. Furthermore, the three-point parameters have been computed for a variety of two-phase model microstructures derived from level cuts of certain Gaussian random fields [57,58,71].

More recently, the parameter ζ_p has been used to model accurately the effective diffusion properties of chromatography columns whose microstructures consist of disordered packings of spherical beads [72–74]. The parameters ζ_p and η_p have also been used to predict the effective thermal conductivity and thermo-mechanical properties of random

[1] A bicontinuous microstructure is one in which both phases are topologically connected across the sample. While this topological feature (i.e., percolation of both phases) is common in 3D systems, it is rare in 2D ones [1].

packings of spheres [75], ellipsoids, and Platonic solids [76]. Beyond simulated microstructures, the parameters ζ_p and η_p have been readily obtained from experimentally obtained disordered microstructural data; including that of binary metal alloys [77,78], Fontainebleau sandstone [79], bicontinuous boron carbide aluminum composites [80], and certain polymer matrix composites [81].

Since the parameters ζ_p and η_p depend on the three-point correlation function, which is generally not known analytically for most microstructures [1,28,55,82–86], they must be ascertained from microstructural samples using computationally demanding methods [1, 28,50,55,69,82–85,87]. Thus, the aforementioned set of microstructures for which ζ_p and η_p have been ascertained was mainly constrained to those consisting of a discrete particle phase embedded in a matrix phase.[2] Here, we overcome such stumbling blocks by using a novel, massively-parallel Monte Carlo integration scheme to compute the parameters ζ_p and η_p for microstructures with much more complex phase geometries and topologies. Specific details of our algorithm and how it improves upon the computational speed and accuracy of previous methods [38,39,49,50,85], are provided in Section 4.

To facilitate selection of a more comprehensive set of microstructures that span the order–disorder spectrum, we leverage the hyperuniformity concept which generalizes the traditional notion of long-range order to not only include all perfect crystals and quasicrystals, but also exotic amorphous states of matter[3] [91,94]. Furthermore, the hyperuniformity concept has led to a unified means to classify two-phase heterogeneous materials, whether hyperuniform or not, according to their large-scale volume fraction fluctuation characteristics [9,92,94,95]. Disordered hyperuniform materials, in particular, possess a hidden form of long-range order in which the material is not crystalline but globally uniform [94]. As they can be endowed with novel directionally independent physical properties that are robust with respect to defects [16,18–20,96–119], disordered hyperuniform materials are receiving considerable attention [7,100,107,111, 112,118,120–136]. For comprehensive reviews on hyperuniformity and hyperuniform materials, the reader is referred to Refs. [94,137].

Here, we specifically study the effective conductivities and elastic moduli of various hyperuniform and nonhyperuniform disk and sphere packings, nonhyperuniform dispersions of certain fully penetrable disks, spheres, ellipses, and ellipsoids, as well as 2D and 3D nonhyperuniform packings of hard platelets, effectively disordered hyperuniform networks and foams, and a model nonhyperuniform phase-inversion symmetric microstructure (see Section 3 for details). Our results indicate that the parameters ζ_2 and η_2 for the microstructures considered here are generally larger for those whose domains of phase 2 are more ramified and well-connected and phase 1 domains are more compact and disconnected for a given volume fraction.

Via the aforementioned microstructure-specific effective property approximations to these models and numerical simulations, we observe that these models can exhibit markedly different effective conductive and mechanical properties. In particular, stealthy hyperuniform packings of disks and spheres (see Sections 3 and 2.2 for details) as well as certain equilibrium hard disk and sphere packings nearly realize the Hashin–Shtrikman lower bounds on the effective conductivity and elastic moduli across volume fractions. We also find that the 2D disordered networks nearly realize the Hashin–Shtrikman upper bounds across volume fractions on the conductivity and bulk modulus, while the 3D foams nearly realize those on the conductivity, bulk, and shear moduli. We discuss how such extremal (i.e., close to Hashin–Shtrikman bounds) effective properties in these models are attributable to certain geometrical and topological characteristics of their microstructures.

The rest of the paper is organized as follows: in Section 2, we provide basic definitions and key background information. Section 3 describes the microstructures that we examine. Our method for computing the three-point parameters is described in Section 4. The main results of the paper are presented in Section 5. Future research directions and conclusions are discussed in Section 6.

2. Definitions and background

In this section, we introduce key concepts and definitions used to describe two-phase microstructures; including the n-point correlation functions, spectral density, local volume fraction fluctuations, and hyperuniformity. Additionally, we briefly summarize the strong-contrast formalism and the three-point microstructural parameters ζ_p and η_p.

2.1. Correlation functions

A two-phase heterogeneous microstructure in d-dimensional Euclidean space $\mathbb{R}^d$ is uniquely determined by the indicator functions $I^{(p)}(\mathbf{x})$ for the individual discrete phases which are defined as

$$I^{(p)}(\mathbf{x}) = \begin{cases} 1, & \mathbf{x} \text{ in phase } p \\ 0, & \mathbf{x} \text{ otherwise} \end{cases}, \tag{1}$$

where $p = 1, 2$ and $\mathbf{x}$ is a position vector [1]. The n-point correlation function $S_n^{(i)}$ for phase p is defined as [1]

$$S_n^{(p)}(\mathbf{x}_1, \mathbf{x}_2, \dots, \mathbf{x}_n) = \left\langle \prod_{j=1}^{n} I^{(p)}(\mathbf{x}_j) \right\rangle \tag{2}$$

where the angular brackets denote an ensemble average. The quantity $S_n^{(i)}(\mathbf{x}_1, \mathbf{x}_2, \dots, \mathbf{x}_n)$ may be interpreted as the probability of finding the endpoints of all vectors $\mathbf{x}_1, \dots, \mathbf{x}_n$ in phase p. Using the expression (2), we can write the one-point correlation function as [1]

$$S_1^{(p)} = \langle I^{(p)}(\mathbf{x}) \rangle \tag{3}$$

which is equal to the volume fraction of phase p, ϕ_p. The two-point correlation function is similarly written as

$$S_2^{(p)}(\mathbf{x}_1, \mathbf{x}_2) = \langle I^{(p)}(\mathbf{x}_1) I^{(p)}(\mathbf{x}_2) \rangle. \tag{4}$$

For statistically homogeneous and isotropic two-phase materials in which there are no preferred centers or directions, this quantity is only dependent on the magnitude of the relative displacement vector $r \equiv |\mathbf{r}| = |\mathbf{x}_2 - \mathbf{x}_1|$ and thus $S_2^{(i)}(\mathbf{x}_1, \mathbf{x}_2) = S_2^{(p)}(r)$ [1]. The three-point correlation function is written as

$$S_3^{(p)}(\mathbf{x}_1, \mathbf{x}_2, \mathbf{x}_3) = \langle I^{(p)}(\mathbf{x}_1) I^{(p)}(\mathbf{x}_2) I^{(p)}(\mathbf{x}_3) \rangle, \tag{5}$$

and can be interpreted as the probability that triangle vertices $\mathbf{x}_1$, $\mathbf{x}_2$, and $\mathbf{x}_3$ all fall in phase p when placed randomly in the system [1]. For statistically homogeneous and isotropic systems, $S_3^{(p)}$ depends only on the magnitudes of the relative displacements of the sampling points, i.e., $S_3^{(p)}(\mathbf{x}_1, \mathbf{x}_2, \mathbf{x}_3) \equiv S_3^{(p)}(r, s, t)$, where $r = |\mathbf{x}_2 - \mathbf{x}_1|$, $s = |\mathbf{x}_3 - \mathbf{x}_1|$, and $t = |\mathbf{x}_3 - \mathbf{x}_2|$.

Note that a two-phase microstructure is said to be phase-inversion symmetric if the morphology of phase 1 at volume fraction ϕ_1 is statistically identical to that of phase 2 in the system where the volume fraction of phase 1 is $1 - \phi_1$ [1], i.e.,

$$S_n^{(1)}(\mathbf{x}^n; \phi_1, \phi_2) = S_n^{(2)}(\mathbf{x}^n; \phi_2, \phi_1), \ n \geq 2. \tag{6}$$

An important property of such phase-inversion symmetric microstructures is that for $\phi_1 = \phi_2 = 1/2$ one can determine the odd-order probability functions $S_{2m+1}^{(p)}$ from $S_{2m}^{(p)}, S_{2m-1}^{(p)}, \dots, S_1^{(p)}$. For the three-point correlation function, we specifically have

$$S_3^{(p)}(r, s, t) = \frac{1}{2}\left[S_2^{(p)}(r) + S_2^{(p)}(s) + S_2^{(p)}(t) - \frac{1}{2}\right]. \tag{7}$$

[2] Such models often require relatively less computational resources to generate [1] or, in certain cases, their three-point correlation functions are known exactly or to a good approximation [1,63,88–90].

[3] Disordered hyperuniformity was first observed in certain exotic point patterns [91] and subsequently generalized to treat two-phase heterogeneous media [92] as well as scalar and vector fields [93].

The autocovariance function is trivially related to the two-point function as [1]

$$\chi_V(\mathbf{r}) \equiv S_2^{(p)}(\mathbf{r}) - \phi_p^2. \tag{8}$$

We define the spectral density $\tilde{\chi}_V(\mathbf{k})$ as the Fourier transform of the autocovariance function at wavevector $\mathbf{k}$, i.e.,

$$\tilde{\chi}_V(\mathbf{k}) = \frac{1}{(2\pi)^d} \int_{\mathbb{R}^d} \chi_V(\mathbf{r}) e^{i\mathbf{k}\cdot\mathbf{r}} d\mathbf{k}. \tag{9}$$

The spectral density is a nonnegative real-valued function of wavevector $\mathbf{k}$ which is directly measurable in the laboratory from elastic scattering experiments [12].

2.2. Classification of hyperuniform and nonhyperuniform materials

We will assume statistically homogeneous two-phase microstructures whose spectral densities exhibit the power-law form

$$\tilde{\chi}_V(\mathbf{k}) \sim B|\mathbf{k}|^\alpha \tag{10}$$

in the limit $|\mathbf{k}| \to 0$. The hyperuniformity of two-phase heterogeneous materials in d-dimensional space is defined by the following infinite-wavelength condition on the spectral density $\tilde{\chi}_V(\mathbf{k})$ [92,94]:

$$\lim_{|\mathbf{k}|\to 0} \tilde{\chi}_V(\mathbf{k}) = 0. \tag{11}$$

Equivalently, one can define hyperuniformity using the local volume fraction variance $\sigma_V^2(R)$ associated with a d-dimensional spherical observation window of radius R [9,92,94]. Specifically, a two-phase material is hyperuniform if its variance $\sigma_V^2(R)$ decays in the large-R limit *faster* than R^{-d}, i.e., faster than the inverse of the spherical observation window volume. This behavior contrasts that of typical disordered two-phase materials for which the variance decays in the large-R limit like R^{-d}.

The hyperuniformity concept provides a unified means to classify material microstructures, hyperuniform or not, according to their large-scale volume fraction fluctuation characteristics. Specifically, there are three different classes (scaling regimes) that describe the associated large-R behaviors of $\sigma_V^2(R)$ when the spectral density goes to zero as a power-law scaling (10) in the limit $|\mathbf{k}| \to 0$ [92,94]:

$$\sigma_V^2(R) \sim \begin{cases} R^{-(d+1)}, & \alpha > 1 \quad \text{(Class I)} \\ R^{-(d+1)} \ln R, & \alpha = 1 \quad \text{(Class II)} \\ R^{-(d+\alpha)}, & 0 < \alpha < 1 \quad \text{(Class III)}. \end{cases} \tag{12}$$

Classes I and III are the strongest and weakest forms of hyperuniformity, respectively. Class I materials include all perfect crystals, many quasicrystals and exotic disordered materials [94]. Also belonging to class I are stealthy hyperuniform materials which are defined to be those which exhibit zero-scattering intensity for a set of wave vectors around the origin [95]:

$$\tilde{\chi}_V(\mathbf{k}) = 0 \qquad \text{for} \quad 0 \le |\mathbf{k}| \le K. \tag{13}$$

Examples of such stealthy materials are periodic packings of disks and spheres, disordered disk and sphere packings derived from stealthy point patterns, as well as specially designed stealthy hyperuniform dispersions [10,11,95,108,109,138]. A sample image of such a stealthy hard disk packing is shown in Fig. 1(a).

Any statistically homogeneous nonhyperuniform two-phase material has a local variance with the following large-R scaling behaviors [139]:

$$\sigma_V^2(R) \sim \begin{cases} R^{-d}, & \alpha = 0 \quad \text{(typical nonhyperuniform)} \\ R^{-(d+\alpha)}, & -d < \alpha < 0 \quad \text{(antihyperuniform)}. \end{cases} \tag{14}$$

A typical nonhyperuniform material has $\tilde{\chi}_V(0) > 0$ and thus $B = \tilde{\chi}_V(0)$ via Eq. (10) [94]. The spectral density of antihyperuniform systems is unbounded at the origin [139]:

$$\lim_{|\mathbf{k}|\to 0} \tilde{\chi}_V(\mathbf{k}) \to +\infty, \tag{15}$$

thus making such systems diametrically opposed to hyperuniform ones. Examples of antihyperuniform systems include systems at thermal critical points (e.g., liquid-vapor and magnetic critical points) [140,141], fractals [142], disordered nonfractals [143], and certain substitution tilings [144].

2.3. Strong contrast expansions and the three-point microstructural parameters

Torquato derived strong-contrast expansions for the effective thermal/electrical conductivity σ_e (and the effective diffusion coefficient D_e, dielectric constant ϵ_e, and magnetic permeability μ_e by mathematical analogy) of two-phase media in any space dimension d [1,28] that may be viewed as *two different expansions* that perturb around the optimal structures that realize the Hashin–Shtrikman (HS) upper bounds. Thus, the first few terms of this expansion, beyond the second-order HS terms, should yield an excellent approximation of σ_e for any values of the phase conductivities for dispersions in which the inclusions are prevented from forming large clusters. In particular, its truncation after third-order terms yields the expression [28]

$$\sigma_e(\sigma_q, \sigma_p, \phi_p, \zeta_p) = \frac{\sigma_q\left(1 + (d-1)\phi_p\beta_{pq} - (d-1)\phi_q\zeta_p\beta_{pq}^2\right)}{1 - \phi_p\beta_{pq} - (d-1)\phi_q\zeta_p\beta_{pq}^2} \tag{16}$$

in which p and q denote the two different phases 1 or 2 such that $p \neq q$, the "polarizability" $\beta_{pq} = (\sigma_p - \sigma_q)/(\sigma_p + (d-1)\sigma_q)$, and ζ_p is a three-point microstructural parameter which is defined for 2D microstructures as

$$\zeta_p = \frac{4}{\pi\phi_1\phi_2} \int_0^\infty \frac{dr}{r} \int_0^\infty \frac{ds}{s} \int_0^\pi d\theta \cos(2\theta) \left[S_3^{(p)}(r,s,\theta) - \frac{S_2^{(p)}(r) S_2^{(p)}(s)}{S_1^{(p)}} \right], \tag{17}$$

and for 3D microstructures as

$$\zeta_p = \frac{9}{2\phi_1\phi_2} \int_0^\infty \frac{dr}{r} \int_0^\infty \frac{ds}{s} \int_{-1}^1 d(\cos\theta) P_2(\cos\theta) \left[S_3^{(p)}(r,s,\theta) - \frac{S_2^{(p)}(r) S_2^{(p)}(s)}{S_1^{(p)}} \right]. \tag{18}$$

In the integrals (17) and (18), the variable θ is related to the arguments of $S_3^{(p)}$, i.e., r, s, and t, via the expression $\theta = \cos^{-1}\left((r^2 + s^2 - t^2)/(2rs)\right)$. Note that $0 \le \zeta_p \le 1$ and that $\zeta_1 + \zeta_2 = 1$. Additionally, plugging in the expression for $S_3^{(p)}$ for phase-inversion symmetric microstructures with $\phi_1 = \phi_2 = 1/2$ (i.e., Eq. (7)) into the integrals (17) and (18) results in $\zeta_2 = 1/2$ in both 2D and 3D.

The approximation (16) has been shown to provide highly accurate approximations of σ_e for a large class of ordered and disordered dispersions in which the particles (phase p) do not form very large clusters for all phase conductivity contrast ratios $\gamma = \sigma_2/\sigma_1$ [1,28]. Note that when $\sigma_2 \ge \sigma_1$, $\sigma_e(\sigma_1, \sigma_2, \phi_2, \zeta_2)$ obtained from Eq. (16) perturbs around the HS lower-bound structures in which the dispersed phase is more conductive than the connected matrix phase. In the phase-interchanged case (i.e., $\sigma_e(\sigma_2, \sigma_1, \phi_1, \zeta_1)$), however, Eq. (16) perturbs around the HS upper-bound structures in which the dispersed phase is less conductive than the matrix phase.

Torquato [1] also derived a different strong-contrast expansion for σ_e that perturbs about microstructures that realize the well-known self-consistent (SC) formula [145–147]. When truncated after third order terms, this expansion yields the formula [1]

$$\phi_2 \frac{\sigma_e + (d-1)\sigma_1}{\sigma_e - \sigma_1} + \phi_1 \frac{\sigma_e + (d-1)\sigma_2}{\sigma_e - \sigma_2} = 2 - d - (d-1)\beta_{21}\left[\phi_1\zeta_2 - \frac{\phi_2(1-\zeta_2)}{1 + (d-2)\beta_{21}}\right], \tag{19}$$

which also depends on the three-point parameter ζ_2. Torquato [1] predicted that the three-point approximation (19) should provide good

estimates of σ_e for phase-inversion symmetric microstructures that resemble those that realize the well-known SC formula, a key feature being phase-inversion symmetry. Henceforth, we refer to Eq. (19) as the "self-consistent" strong-contrast approximation. In a forthcoming manuscript, we show that Eq. (19) accurately approximates the effective conductivities across volume fractions as well as the percolation thresholds of highly clustered 2D and 3D microstructures, including a symmetric cell material, a disordered phase inversion symmetric microstructure, and certain dispersions of overlapping particles [148].

Note that the parameter ζ_2 also appears in the best available three-point "Beran-type" lower and upper bounds on the effective conductivity [24,27,36,37,149,150], i.e., $\sigma_L^{(3)} \le \sigma_e \le \sigma_U^{(3)}$ where

$$\sigma_L^{(3)} = \langle\sigma\rangle - \frac{\phi_1\phi_2(\sigma_2-\sigma_1)^2}{\langle\tilde{\sigma}\rangle + (d-1)\langle\sigma^{-1}\rangle_\zeta^{-1}}, \tag{20}$$

and

$$\sigma_U^{(3)} = \langle\sigma\rangle - \frac{\phi_1\phi_2(\sigma_2-\sigma_1)^2}{\langle\tilde{\sigma}\rangle + (d-1)\langle\sigma\rangle_\zeta}, \tag{21}$$

respectively, in which $\langle\sigma\rangle = \phi_1\sigma_1 + \phi_2\sigma_2$, $\langle\tilde{\sigma}\rangle = \phi_2\sigma_1 + \phi_1\sigma_2$, and $\langle c\rangle_\zeta = c_1\zeta_1 + c_2\zeta_2$. By incorporating three-point microstructural information via the parameter ζ_2, these bounds improve upon the well-known Hashin–Shtrikman lower and upper bounds [43,46], i.e.,

$$\sigma_L^{(2)} = \langle\sigma\rangle - \frac{\phi_1\phi_2(\sigma_2-\sigma_1)^2}{\langle\tilde{\sigma}\rangle + (d-1)\sigma_1}, \tag{22}$$

and

$$\sigma_U^{(2)} = \langle\sigma\rangle - \frac{\phi_1\phi_2(\sigma_2-\sigma_1)^2}{\langle\tilde{\sigma}\rangle + (d-1)\sigma_2}, \tag{23}$$

respectively. The bounds (22) and (23) are d-dimensional generalizations of the HS bounds derived by Torquato [1]. Note that when $\zeta_2 = 0$, the three-point bounds (20) and (21) coincide and equal the two-point HS lower bound (22) for $\sigma_2 \ge \sigma_1$. When $\zeta_2 = 1$, the three-point bounds coincide and equal the HS upper bound (23) for $\sigma_2 \ge \sigma_1$. Examples of microstructures that realize the d-dimensional HS bounds on σ_e are the well-known singly coated d-dimensional sphere assemblies [43,151] and rank-d laminates [152,153]. Note that for either the coated-inclusion assemblies or finite-rank laminates, one of the phases is always a disconnected dispersed phase within a connected matrix phase, except in the trivial case when the dispersed phase fills all of space [1].

Torquato [1,28] has shown that the three-point approximation Eq. (16) always lies between the best available rigorous three-point bounds (20) and (21) on the effective conductivity provided that

$$\zeta_2 \le \frac{1}{d-1}. \tag{24}$$

In our forthcoming manuscript [148], we show analytically that the "self-consistent" three-point approximation Eq. (19) for 2D microstructures lies between the three-point bounds (20) and (21) for all values of ζ_2. For general 3D microstructures, analogous constraints on ζ_2 are dependent on the phase conductivity contrast ratio γ as well as the phase 2 volume fraction ϕ_2 and must be determined numerically [148]. For 3D phase-inversion symmetric microstructures, however, we show that Eq. (19) always lies between the three-point bounds provided that $\zeta_2 \le 1/2$ and $\gamma > 1$ [148].

Generalizing the approach used to derive strong-contrast expansions for the effective conductivity, Torquato derived analogous contrast expansions for the effective stiffness tensor $\mathbf{C}_e$ of two-phase media in any space dimension d [23,30,31]. As with the effective conductivity, these expansions may be viewed as two different expansions that perturb about the HS optimal structures, and thus the first few terms of this expansion should yield an excellent approximation of $\mathbf{C}_e$ for dispersions in which the inclusions are prevented from forming large clusters. Truncation after third-order terms specifically yields the approximations

$$\phi_p\frac{\kappa_{pq}}{\kappa_{eq}} = 1 - \frac{(d+2)(d-1)G_q\kappa_{pq}\mu_{pq}}{d(K_q+2G_q)}\phi_q\eta_p, \tag{25}$$

and

$$\phi_p\frac{\mu_{pq}}{\mu_{eq}} = 1 - \frac{2G_q\kappa_{pq}\mu_{pq}}{d(K_q+G_q)}\phi_q\zeta_p - \frac{1}{2d}\left[\frac{dK_q+(d-2)G_q}{K_q+2G_q}\right]^2\mu_{pq}^2\phi_q\eta_p, \tag{26}$$

for the effective bulk K_e and shear G_e moduli, respectively. In Eqs. (25) and (26), the scalar polarizabilities are defined as $\kappa_{pq} = (K_p - K_q)/(K_p + 2(d-1)G_q/d)$ and

$$\mu_{pq} = \frac{G_p - G_q}{G_q}\frac{1}{1+\frac{dK_q/2+(d+1)(d-2)G_q/d}{K_q+2G_q}}, \tag{27}$$

and the three-point parameter η_p for 2D and 3D microstructures is given by the integrals

$$\eta_p = \frac{16}{\pi\phi_1\phi_2}\int_0^\infty\frac{dr}{r}\int_0^\infty\frac{ds}{s}\int_0^\pi d\theta\cos(4\theta)\left[S_3^{(p)}(r,s,\theta) - \frac{S_2^{(p)}(r)S_2^{(p)}(s)}{S_1^{(p)}}\right], \tag{28}$$

and

$$\eta_p = \frac{5\zeta_p}{21} + \frac{150}{7\phi_1\phi_2}\int_0^\infty\frac{dr}{r}\int_0^\infty\frac{ds}{s}\int_{-1}^1 d\theta P_4(\cos\theta)\left[S_3^{(p)}(r,s,\theta) - \frac{S_2^{(p)}(r)S_2^{(p)}(s)}{S_1^{(p)}}\right], \tag{29}$$

respectively. As with the parameter ζ_p, $0 \le \eta_p \le 1$, $\eta_1 + \eta_2 = 1$, and phase-inversion symmetric microstructures with $\phi_1 = \phi_2 = 1/2$ will also have $\eta_2 = 1/2$.

The three-point approximations (25) and (26) have been shown to accurately approximate the effective elastic moduli of dispersions for all phase contrasts, provided that the particles (phase p) generally do not form large clusters [31]. Note that when phase p is stiffer than phase q such that $(K_p - K_q)(G_p - G_q) \ge 0$, Eqs. (25) and (26) perturb around the HS lower-bound structures when phase p is the dispersed phase and phase q is the matrix phase. In the phase-interchanged case, however, these approximations perturb around HS upper-bound structures when phase p is the matrix phase and phase q is the dispersed phase [1].

The parameters ζ_2 and η_2 also arise in a variety of three-point bounds on the effective elastic moduli. For example, the lower and upper "Beran-type" three-point bounds on the effective bulk modulus for isotropic d-dimensional microstructures (i.e., $K_L^{(3)} \le K_e \le K_U^{(3)}$) are given respectively by [34–36]

$$K_L^{(3)} = \langle K\rangle - \frac{\phi_1\phi_2(K_2-K_1)^2}{\langle\tilde{K}\rangle + 2(d-1)\langle G_\zeta^{-1}\rangle^{-1}/d} \tag{30}$$

and

$$K_U^{(3)} = \langle K\rangle - \frac{\phi_1\phi_2(K_2-K_1)^2}{\langle\tilde{K}\rangle + 2(d-1)\langle G\rangle_\zeta/d}. \tag{31}$$

Analogous bounds for the effective shear modulus (i.e., $G_L^{(3)} \le G_e \le G_U^{(3)}$) are given by [34–36,38]

$$G_L^{(3)} = \langle G\rangle - \frac{\phi_1\phi_2(G_2-G_1)^2}{\langle\tilde{G}\rangle + \Xi}, \tag{32}$$

and

$$G_U^{(3)} = \langle G\rangle - \frac{\phi_1\phi_2(G_2-G_1)^2}{\langle\tilde{G}\rangle + \Theta}, \tag{33}$$

in which

$$\Xi \equiv \begin{cases} \left(2\langle 1/k\rangle_\zeta + \langle 1/G\rangle_\eta\right)^{-1}, & d=2 \\ \dfrac{\left\langle \frac{128}{K}+\frac{99}{G}\right\rangle_\zeta + 45\left\langle \frac{1}{G}\right\rangle_\eta}{30\left\langle \frac{1}{G}\right\rangle_\zeta \left\langle \frac{6}{K}-\frac{1}{G}\right\rangle_\zeta + 6\left\langle \frac{1}{G}\right\rangle_\eta \left\langle \frac{2}{K}+\frac{21}{G}\right\rangle_\zeta}, & d=3, \end{cases} \tag{34}$$

and

$$\Theta \equiv \begin{cases} \dfrac{2\langle k\rangle_\zeta \langle G\rangle^2 + \langle k\rangle^2 \langle G\rangle_\eta}{\langle k+2G\rangle^2}, & d=2 \\ \dfrac{3\langle G\rangle_\eta \langle 6K+7G\rangle_\zeta - 5\langle G\rangle_\zeta^2}{6\langle 2K-G\rangle_\zeta + 30\langle G\rangle_\eta}, & d=3. \end{cases} \tag{35}$$

For 2D composites, note that Gibiansky and Torquato [41] improved upon the upper bound (31) on the effective planar bulk modulus k_e as well as that (33) on the effective transverse shear modulus G_e (these improved bounds also depend on the parameters ζ_2 and η_2). Also note that all of the aforementioned two- and three-point bounds on the effective bulk and shear moduli assume the "well-ordered" case in which $(K_2 - K_1)(G_2 - G_1) \geq 0$. By incorporating microstructural information at the three-point level via the parameters ζ_p and η_p, the aforementioned three-point bounds improve upon well-known Hashin–Shtrikman ones [44,45], i.e.,

$$K_L^{(2)} = \langle K\rangle - \frac{\phi_1\phi_2(K_2-K_1)^2}{\langle \tilde{K}\rangle + 2(d-1)G_1/d}, \tag{36}$$

$$K_U^{(2)} = \langle K\rangle - \frac{\phi_1\phi_2(K_2-K_1)^2}{\langle \tilde{K}\rangle + 2(d-1)G_2/d}, \tag{37}$$

$$G_L^{(2)} = \langle G\rangle - \frac{\phi_1\phi_2(G_2-G_1)^2}{\langle \tilde{G}\rangle + H_1}, \tag{38}$$

and

$$G_U^{(2)} = \langle G\rangle - \frac{\phi_1\phi_2(G_2-G_1)^2}{\langle \tilde{G}\rangle + H_2}, \tag{39}$$

in which

$$H_i \equiv G_i\left[\frac{dK_i/2 + (d+1)(d-2)G_i/d}{K_i + 2G_i}\right]. \tag{40}$$

Note that the bounds (36), (37), (38) and (39) are d-dimensional generalizations of the HS bounds derived by Torquato [1]. When $\zeta_2 = 0$, the three-point bounds (30) and (31) on K_e coincide and equal the two-point HS lower bound (22) for $G_2 \geq G_1$. When $\zeta_2 = 1$, the three-point bounds on K_e coincide and equal the two-point HS upper bound (23) for $G_2 \geq G_1$. Similarly, when $\zeta_2 = 0$ and $\eta_2 = 0$, the three-point bounds (32) and (33) on G_e coincide and equal the two-point HS upper bound (38) when $G_2 \geq G_1$ and $K_2 \geq K_1$. Lastly, the three-point bounds on G_e coincide and equal the HS upper bound (39) when $\zeta_2 = 1$, $\eta_2 = 1$, $G_2 \geq G_1$ and $K_2 \geq K_1$. As with the effective conductivity, the Hashin–Shtrikman bounds on K_e are attained by the aforementioned singly coated d-dimensional sphere assemblies [44] and certain finite-rank laminates [154]. While the sphere assemblies do not realize the HS bounds on G_e [155], these bounds are realized by various laminate constructions [154,156–158].

Torquato [31] has shown analytically that the three-point approximations of the effective bulk modulus (25) for 2D composites lies between the best available three-point bounds (i.e., the lower bound (30) and the Gibiansky-Torquato upper bound [41]) provided that $\zeta_2 < 1/2$. For 3D microstructures, he found Eq. (25) lies between the best available three-point bounds (i.e., (30) and (31)) provided that

$$\zeta_2 \leq \begin{cases} 0.6 + \frac{8G_1}{15K_1}, 0 \leq G_1/K_1 \leq 3/4 \\ 1, G_1/K_1 > 3/4. \end{cases} \tag{41}$$

No such analytical expressions exist for the effective shear modulus (26), but the corresponding constraints on ζ_2 and η_2 may be ascertained numerically as described in Ref. [31].

Table 1
The list of abbreviations and dimensions for the model microstructures considered in this paper. For all models consisting of particles embedded in a matrix, we take the particles to be phase 2 and the matrix to be phase 1. The walls/struts of the networks and foams are taken to be phase 2.

Model Name	Abbreviation	Dimension, d
Fully Penetrable Disks/Spheres	FPD/S	2, 3
Fully Penetrable Ellipses/Oblate Ellipsoids	FPE/E	2, 3
Equilibrium Hard Disks/Spheres	EHD/S	2, 3
Metastable Hard Spheres	MHS	2
$\chi = 0.002$ Stealthy Disk/Sphere Packings	SHU ($\chi = 0.002$)	2, 3
$\chi = 0.45$ Stealthy Disk/Sphere Packings	SHU ($\chi = 0.45$)	2, 3
Hard Platelets	PLT	2, 3
Thickened networks derived from $\chi = 0.48$ stealthy point patterns	SHU-NET	2, 3
Closed-cell foam microstructures derived from $\chi = 0.48$ stealthy point patterns	SHU-FOAM	3
Debye random media	DRM	2, 3

3. Model microstructures

In this section, we summarize the salient details of the 2D and 3D hyperuniform and nonhyperuniform model microstructures that we consider in this paper. These models constitute a representative set of material microstructures that span the order–disorder spectrum according to order metrics that we recently developed [9]. The complete set of models and the abbreviations that we use to denote them are listed in Table 1. All models considered here are subject to periodic boundary conditions.

3.1. Fully penetrable disks, spheres, ellipses, and oblate ellipsoids

We consider the well-known fully penetrable disk and sphere model microstructures [1,159]. These model nonhyperuniform [9] systems are prepared by decorating the points of a Poisson point process with d-dimensional radius a spheres that are free to overlap with one another. We note that volume fraction ϕ_2 of the disk/sphere phase of these systems is given by $\phi_2 = \exp[-\rho v_1(a)]$, in which ρ is the number density of the underlying Poisson point pattern and $v_1(a)$ is the volume of a d-dimensional sphere of radius a [1,159]. While the parameters ζ_2 and η_2 have already been computed for these models [53,55,83], they serve as useful benchmarks for our algorithm (see Section 4 and the Supporting Information for details).

To characterize the effect of particle-shape on the parameters ζ_2 and η_2, we also consider dispersions of fully penetrable elongated ellipses (ratio of axes $b/a = 5$) as well as oblate ellipsoids (ratio of axes $b/a = 1$ and $b/c = 5$). For these models, we use the minor-axis a as the characteristic length scale of the microstructure. These systems are prepared analogously to the fully penetrable disk and sphere systems, except here one assigns a random orientation to each particle. By virtue of having no long-range spatial or orientational correlations, these systems are very likely nonhyperuniform. For these models, the volume fraction is given by the expression $\phi_2 = \exp[-\rho v_E]$ in which v_E is the volume of the ellipses/ellipsoids decorating each point [160]. For all fully penetrable particle models considered here, we generate systems comprised of $N = 2500$ particles with phase 2 volume fractions $0.05 \leq \phi_2 \leq 0.95$. Sample images of fully penetrable disk and ellipse microstructures are shown in Figs. 1(b) and 1(c), respectively.

3.2. Equilibrium and metastable hard disk and sphere packings

We also consider equilibrium (Gibbs) ensembles of identical nonoverlapping disks and spheres of radius a across their respective stable fluid, freezing, and crystalline branches. These nonhyperuniform [91] systems display a wide-array of microstructural geometries and topologies all the way up to their respective maximal packing fractions,

i.e., $\phi_2 = 0.907$ for disks and $\phi_2 = 0.74$ for spheres [1]. We specifically prepare configurations of $N = 2340$ disks with packing fractions in the range $0.5 \le \phi_2 \le 0.90$ and $N = 2916$ spheres with $0.5 \le \phi_2 \le 0.70$ using the event-driven molecular dynamics simulation code from Ref. [161]. Additionally, we also generate configurations of $N = 3000$ hard spheres along the metastable fluid branch (i.e., $0.49 < \phi_2 < 0.64$ [1]) using the procedure described in Ref. [162]. Note that the values of ζ_2 and η_2 for the disordered fluid branches of the equilibrium hard disk and sphere systems were previously obtained using certain approximations of the three-point correlation functions for these systems [59,64,163,164].

3.3. Disordered hard platelet packings

As a contrast to the various hard disk and sphere systems considered here, we also examine certain non-equilibrium packings of randomly oriented hard platelet-shaped particles in 2D and 3D [165]. We specifically model the platelets as oblate super ellipsoids [166] whose domains are defined by the inequality

$$\left|\frac{x}{a}\right|^{2p} + \left|\frac{y}{b}\right|^{2p} + \left|\frac{z}{c}\right|^{2p} \le 1, \tag{42}$$

in which the parameters a, b, and c are the three semi-axes of the super ellipsoid and the parameter $p \ge 0$ is the deformation parameter, which indicates the extent to which the shape is deformed away from an ellipsoid ($p = 1$). Using an algorithm adapted from Ref. [167], we generate these packings by randomly placing and orienting each platelet in the periodic simulation cell one after another such that there are no overlaps. At the maximal possible packing fraction, no additional particles can be inserted into the system [1]. As packings of disks and spheres prepared by this procedure are nonhyperuniform [91], the platelet packings considered here are also likely to be nonhyperuniform. Here, we specifically consider thin rectangular platelets in 2D by taking the ratio of axes $b/a = 10$, deformation parameter $p = 3$, and setting the variable $z = 0$ in the inequality (42). In 3D, we consider oblate platelets with square faces and thin rectangular sides by taking the ratios of the axes to be $b/a = 1$ and $b/c = 10$ and parameter $p = 3$ in (42), taking the minor semi-axis a as the characteristic length scale for these microstructures. We generate $N = 2500$ packings of such platelets in 2D and 3D with volume fractions in the ranges $0.05 \le \phi_2 \le 0.4594$ and $0.05 \le \phi_2 \le 0.1750$, respectively. A sample image of a 2D platelet packing is shown in Fig. 1(e).

3.4. Stealthy hyperuniform hard disk and sphere packings

We also examine certain disordered stealthy hyperuniform radius a disk and sphere packings which, as a consequence of being stealthy and disordered, can have local clusters of contacting particles that are much smaller than those found in equilibrium packings of the same volume fraction [10,11,19]. These packings are made by decorating certain stealthy hyperuniform point patterns with non-overlapping disks/spheres, as described in Refs. [10,11,19]. We note that such a decoration process exactly preserves the stealthiness of the point pattern [93]. It is useful to describe these point-pattern derived packings in terms of the χ parameter, which is a measure of the size of the stealthy "exclusion region" in which there is zero-scattering intensity around the origin. In particular, the 2D and 3D stealthy systems considered here are highly degenerate and disordered for $0 < \chi < 1/2$, with their degree of short-range order increasing as $\chi \to 1/2$ before crystalline phases emerge for $1/2 < \chi < 1$ [168]. Here, we straddle the disordered regime by examining packings with $\chi = 0.002$ and $\chi = 0.45$. Note that the range of attainable maximal packing fractions for these systems is dependent on both the dimension and the value of χ [10,11]. Thus, for the $\chi = 0.45$ disk and sphere packings ($N = 4000$), we generate systems with packing fractions within the ranges $0.20 \le \phi_2 \le 0.69$ and $0.20 \le \phi_2 \le 0.45$, respectively. For the $\chi = 0.002$, disk and sphere packings ($N = 4000$), we generate systems with packing fractions within the ranges $0.20 \le \phi_2 \le 0.86$ and $0.60 \le \phi_2 \le 0.64$, respectively. The reader is referred to Refs. [10,11,168] for more comprehensive descriptions of stealthy hyperuniformity and these packings. A sample image of $\chi = 0.45$ stealthy hyperuniform disk packing is shown in Fig. 1(a).

3.5. Networks and foams

Additionally, we examine disordered 2D and 3D cellular microstructures derived from $\chi = 0.48$ stealthy hyperuniform point patterns. Not only are the phase connectivity properties of these effectively hyperuniform microstructures unique among the models considered here, but certain 2D networks derived from such stealthy point patterns were shown to possess virtually optimal effective properties for $\phi_2 \ll 1$ [119]. We prepare trivalent 2D and tetravalent 3D network two-phase microstructures by decorating the edges of the Delaunay-centroidal tessellations of $\chi = 0.48$ stealthy point patterns with walls of width w and cylinders of radius a, respectively [16,133]. As a contrast to the *open-cell* 3D networks, we also prepare topologically distinct 3D *closed-cell* foams by thickening the walls of the cells of the Voronoi tessellations [169] of the same $\chi = 0.48$ stealthy point patterns. In all cases, the relationships between the wall widths w/strut radii a (which we use as characteristic length scales) and ϕ_2 must be determined empirically. Here, the 2D networks ($N = 3000$ cells) have wall phase volume fractions $0.05 \le \phi_2 \le 0.75$.[4] Both the 3D network and foam microstructures ($N = 500$ cells) have strut/wall phase volume fractions $0.05 \le \phi_2 \le 0.95$. A sample image of a 2D disordered network microstructure is shown in Fig. 1(f).

3.6. Phase-inversion symmetric Debye random media

Debye random media are nonhyperuniform [9,32] models of two-phase media which are defined entirely by the autocovariance function

$$\chi_V(r) = \phi_1\phi_2 \exp(-r/a), \tag{43}$$

in which $a > 0$ is the characteristic length scale of the microstructure. The simple exponential form (43) was hypothesized by Debye et al. to model 3D microstructures with phases of "fully random shape, size, and distribution" [12], and were shown to be realizable in two [13] and three [32] dimensions. We consider Debye random media here as they have been shown to be a good approximation of certain microstructures [12], including Fontainebleau sandstone [79]. By virtue of being phase-inversion symmetric, Debye random media also serve as a useful testbed for the "self-consistent" three-point approximation formula for the effective conductivity (19). Here, we generate 2D 1024×1024 pixel and 3D $192 \times 192 \times 192$ voxel realizations of Debye random media with volume fractions $0.05 \le \phi_2 \le 0.95$ using the Fourier-based microstructure reconstruction algorithm described in Ref. [109]. We set the parameter $a = 10$ pixels and $a = 5$ voxels in 2D and 3D reconstructions, respectively. A sample image of 2D Debye random media is shown in Fig. 1(d).

4. Methodology to compute three-point parameters

In this section, we describe in detail our Monte Carlo integration methodology that we use to compute ζ_p and η_p. Our method specifically utilizes the following approximation of the three-point parameter integrals (17), (18), (28), and (29):

$$X_{p,n} = \frac{V_d}{N_V N_S V \pi} \sum_{i=1}^{N_V} \sum_{j=1}^{N_S^{(i)}} \mathcal{I}^{(p)}(\mathbf{x}_{ij}) \times$$

[4] The walls of networks with $\phi_2 > 0.75$ would fill entire cells, so these structures were omitted from the present study.

$$\mathcal{I}^{(p)}(\mathbf{x}_{ij}+\mathbf{r}_{ij})\mathcal{I}^{(p)}(\mathbf{x}_{ij}+\mathbf{s}_{ij})f_n(\theta_{ij}), \tag{44}$$

in which V is the volume of the microstructure sample, N_V and V_d are the number and volume of the stratified sub-domains, respectively, $N_S^{(i)}$ is the number of sampling triangles with vertices $(\mathbf{x}_{ij}, \mathbf{x}_{ij}+\mathbf{r}_{ij}, \mathbf{x}_{ij}+\mathbf{s}_{ij})$ in the ith sub-domain, $\cos(\theta_{ij}) = \mathbf{r}_{ij}\cdot\mathbf{s}_{ij}$, and

$$f_n(\theta) = \begin{cases} \cos(n\theta), & d=2 \\ P_n[\cos(\theta)]\sin(\theta), & d=3 \end{cases} \tag{45}$$

where $n = 2$ for ζ_p and $n = 4$ for η_p. Note that we do not include the $S_2^{(p)}(r)S_2^{(p)}(s)/\phi_p$ terms from the three-point parameter integrals in Eq. (44) because they ultimately evaluate to zero.

Stratified sampling [170] is used to prioritize sampling of S_3 in regions of the microstructure that contribute non-trivially to the summation (44). In this scheme, a d-dimensional microstructure is divided uniformly into $N_V = L^d$ hypercubic sub-domains (or strata) of volume V_d. Within each domain i, $N_S^{(i)}$ sampling triangle "anchor points" $\mathbf{x}_{ij}$ are allocated toward computing the inner summation of Eq. (44). By taking $N_S^{(i)}$ to be proportional to the variance of the integrand within sub-domain i, we concentrate samples in regions where the integrand fluctuates the most [171]. We note that the integrand has exactly zero variance whenever the anchor point $\mathbf{x}_{ij}$ is outside of the phase of interest. Therefore, only domains that are at least partially covered by the phase of interest are allocated $N_S > 0$ sampling triangles. Lastly, we ensure that the computational cost of our method is independent of the volume fraction of the microstructure by requiring that the number of sub-domains per side is

$$L = \lceil (N_{ad}/\phi_p)^{1/d} \rceil. \tag{46}$$

In order to improve sampling efficiency, the target number of active domains N_{ad} can be tuned (subject to hardware constraints) such that the strata are comparable in size to the characteristic length scale of the microstructure.

The diverging factors of $1/r$ and $1/s$ in integrals (17), (18), (28) and (29) are eliminated from Eq. (44) via importance sampling of $|\mathbf{r}_{ij}|$ and $|\mathbf{s}_{ij}|$ from the log-uniform distribution [50], i.e.,

$$f(x) = \frac{1}{\ln(x_{max}/x_{min})x}. \tag{47}$$

Here, x_{min} and x_{max} denote the minimum and maximum numerical values of r and s sampled, respectively. Specific choices of these parameters are microstructure-dependent and detailed in Section 5.1.

The jth anchor point of the ith sub-domain $\mathbf{x}_{ij}$ is sampled uniformly within the sub-domain's volume, while the orientation of vector $\mathbf{r}_{ij}$ is randomly sampled from the uniform distribution $\mathcal{U}(0, 2\pi)$. The orientation of vector $\mathbf{s}_{ij}$ relative to $\mathbf{r}_{ij}$ is given by the angle θ_{ij}, which is sampled from a low-discrepancy, or quasirandom, sequence.[5] The values of θ_{ij} are given by the so-called "golden ratio" sequence [172] which is based on the fractional part of successive integer multiples of the golden ratio. Specifically, the jth value of θ in the ith sub-domain is given by:

$$\theta_{ij} = \pi\left\{a_i + \frac{j}{\varphi}\right\}, \tag{48}$$

in which $\{x\}$ denotes the fractional part of x, $\varphi = (1+\sqrt{5})/2$ is the golden ratio, and a_i is a random "seed" for the ith sub-domain sampled from $\mathcal{U}(0, 1)$. The previously outlined steps constitute the generation of the jth sampling triangle within the ith sub-domain for 2D microstructures. For 3D systems, each sampling triangle is rotated via a rotation matrix parameterized with random Euler angles.

[5] Low-discrepancy, or quasirandom, sequences are deterministic point patterns in d-dimensional Euclidean space $\mathbb{R}^d$ that cover space *more uniformly* than a Poisson point pattern of the same density [170].

Unlike other methods for computing ζ_p and η_p, which rely on computer-memory intensive sampling grids [75,76,85,87], the comparatively small memory requirements of computing Eq. (44) make it ideally suited for graphics processing unit (GPU) hardware. Thus, each GPU thread is assigned to a sub-domain so that the inner sum of Eq. (44) is computed in parallel. Note that the error of Monte Carlo integration (i.e., the standard deviation σ_I) decays asymptotically with the number of samples N as $\sigma_I \sim A/\sqrt{N}$ [170]. Overall, we effectively reduce the value of coefficient A by using stratified sampling [170,171], importance sampling [1,170], and low-discrepancy sequences [170]. We gain additional accuracy by simply increasing N, which is accomplished in a computationally efficient manner by our GPU parallelization scheme. Benchmark tests confirming the accuracy of our algorithm are provided in the Supporting Information.

We note that the actual run times of the algorithm ultimately depend on the computational cost of evaluating the indicator function terms $\mathcal{I}^{(p)}(\mathbf{x})$ in summation (44), which will vary depending on how the microstructure is represented numerically. For example, evaluating $\mathcal{I}^{(p)}(\mathbf{x})$ for digitized representations of microstructures (e.g., 2D and 3D Debye random media, as well as the 3D networks and foams) involves a relatively fast $\mathcal{O}(1)$ array lookup. By contrast, the computational cost of evaluating $\mathcal{I}^{(p)}(\mathbf{x})$ for dispersions of discrete particles, which are represented numerically as arrays of particle centroids, dimensions, and orientations, generally scales with the number of particles N as $\mathcal{O}(N)$, although we appreciably speed up these calculations using a cell-list [173]. Thus, evaluating ζ_2 and η_2 using 2^{38} total samples and $N_{ad} = 2^{20}$ active domains takes, on average, 10 min for a 192^3 voxel microstructure and 21 min for a 3D packing of $N = 2500$ hard platelets using a single NVIDIA®A100 GPU, rather than relying on hundreds or thousands of CPU cores like previous methods [50,75,76].

5. Results

5.1. Three-point parameters

In this subsection, we present values of ζ_2 and η_2 obtained via the numerical algorithm described in Section 4 for the model microstructures considered in this paper. For each microstructure, all values of the three-point parameters are averaged over between 10 and 20 different ensembles. A total number of 2^{38} Monte Carlo samples were used for each computed value of ζ_2 and η_2 (i.e., $N_s \times N_V = 2^{38}$ in Eq. (44)). We found that this number of samples was more than sufficient to guarantee convergence of both the ζ_2 and η_2 integrals. For all models, the minimum and maximal values of the lengths r and s in Eq. (44) were taken to be $10^{-5}a$ and $L/8$, respectively, where a is the characteristic length scale of the microstructure and L is the side length of the periodic simulation cell. All numerical values of ζ_2 and η_2 for the model systems considered in this paper are tabulated in the Supporting Information.

Overall, we find that the 2D and 3D models in which phase 2 is more well-connected and ramified and phase 1 is more disconnected and compact tend to have larger values of the three-point parameters for a given volume fraction, as seen in the rank-ordering of microstructures in the plots of ζ_2 and η_2 as functions of ϕ_2 in Figs. 2 and 3, respectively. This relationship between the degree of phase-connectivity and the values of the three-point parameters is expected because, as discussed in Section 2.3, the optimal microstructures with $\zeta_2 = 1$ have phase 1 disconnected and dispersed in phase 2, which is fully connected. For example, the 2D network and 3D foam microstructures (in which phase 1 is always disconnected; see Fig. 1(f)) and the $\chi = 0.45$ stealthy disk and sphere packings (in which phase 2 is always disconnected; see Fig. 1(a)) have the largest and smallest values of ζ_2 and η_2, respectively, for a given value of ϕ_2 among the models considered here.

Specifically, the 2D network and 3D foam microstructures have $\zeta_2 \gtrsim 0.8$ whereas the $\chi = 0.45$ stealthy disk and sphere packings have $\zeta_2 \lesssim 0.2$ across their respective ranges of ϕ_2, as seen in Fig. 2(a).

Similarly, the 3D foam microstructures have $\eta_2 \gtrsim 0.6$ while the stealthy disks and sphere have $\eta_2 \lesssim 0.2$ and $\eta_2 \lesssim 0.5$, respectively, as seen in Fig. 3(a). The non-monotonic dependence of η_2 on ϕ_2 for the 2D networks seen in Fig. 3(a) is a consequence of their tendency to have lower shear moduli and will be elaborated on in Section 5.2. Unlike the 3D foams, the 3D open-cell networks are *bicontinuous* for $0 < \phi_2 < 1$ which is why their ζ_2 and η_2 values are more comparable to the other bicontinuous 3D models (i.e., fully penetrable ellipsoids and spheres, and 3D Debye random media).

For microstructures consisting of particles embedded in a matrix, we find that both more non-spherical inclusion geometries and/or penetrable particles (e.g., see Figs. 1(c) and 1(e)), result in more branched and extended domains of phase 2 and thus larger values of ζ_2 and η_2 than those with circular/spherical inclusions (e.g., see Figs. 1(a) and 1(b)). Specifically, in the plots of ζ_2 for the 2D models in Fig. 2(a), it is seen that the thin, rectangular platelets have ζ_2 that are up to six times larger than those for equilibrium hard disks, while the elongated fully penetrable ellipse systems have ζ_2 that are up to four times larger than those for the fully penetrable disk models for $\phi_2 = 0.05$. Similarly, large differences between the values of η_2 for the aforementioned models are seen in Fig. 3(a). This trend is also observed in the 3D analogues of these models as seen in Figs. 2(b) and 3(b), respectively. Our observations here are consistent with those of Gillman et al., who observed that values of ζ_2 for disordered packings of tetrahedra were up to six times larger than those for random sphere packings for a given volume fraction [76]. Interestingly, 2D and 3D Debye random media have ζ_2 and η_2 that are comparable to those of the fully penetrable ellipse/ellipsoid systems. As we have previously shown that Debye random media are well-approximated by certain systems of fully penetrable polydisperse disks and spheres [15], it is reasonable that fully penetrable ellipses and ellipsoids are also structurally similar to Debye random media.

Interestingly, the 2D and 3D hard platelet systems have ζ_2, and to a lesser extent, η_2 that *decrease* with increasing of ϕ_2. This behavior is attributable to the tendency of the highly nonspherical platelets to aggregate into increasingly more compact clusters due to local nematic ordering as ϕ_2 increases toward its maximal value. Similarly, the drops in ζ_2 and η_2 with increasing ϕ_2 seen in the equilibrium hard disk and sphere systems is a consequence of increased clustering of particles into compact crystalline domains above their respective freezing points $\phi_2^{(f)}$ (i.e., $\phi_2^{(f)} \approx 0.69$ for EHD and $\phi_2^{(f)} \approx 0.49$ for EHS [1]). Note that the clustering associated with this phase-transition does not occur along the metastable branch of the hard sphere fluid or the structurally similar [10,11] $\chi = 0.002$ stealthy sphere packings which is why ζ_2 and η_2 for these structures continue to increase above $\phi_2^{(f)}$. There is also no such freezing transition in the $\chi = 0.002$ stealthy hard disk system [10,11] and thus no corresponding decrease in the values of ζ_2 and η_2 for these systems.

While the rank-ordering of microstructures predicted by ζ_2 and η_2 for the 2D and 3D model systems are generally the same for a given ϕ_2, the spread of the η_2 values is appreciably smaller than that of ζ_2.[6] Thovert et al. observed similar differences between the sizes of ranges of ζ_2 and η_2 values for certain packings of polydisperse hard spheres [66]. As η_2 only appears in approximations of and bounds on the effective shear modulus, a quantity that is not necessarily increased by a high-degree of phase connectivity [1,119,174,175], it is reasonable that this parameter would have a reduced range of values relative to that of ζ_2.

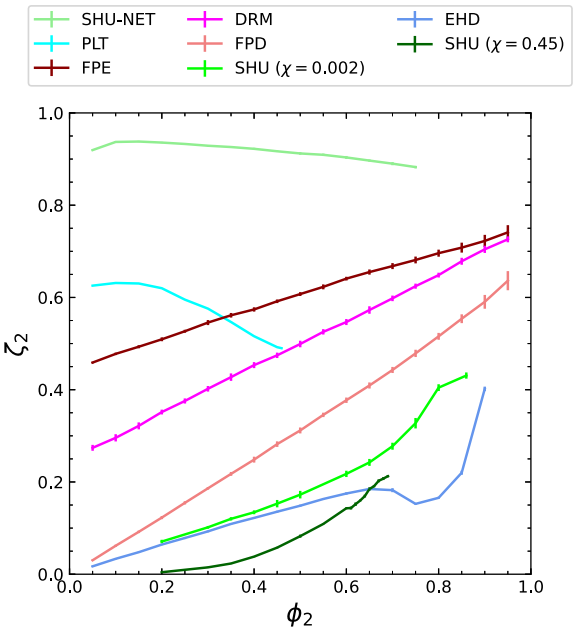
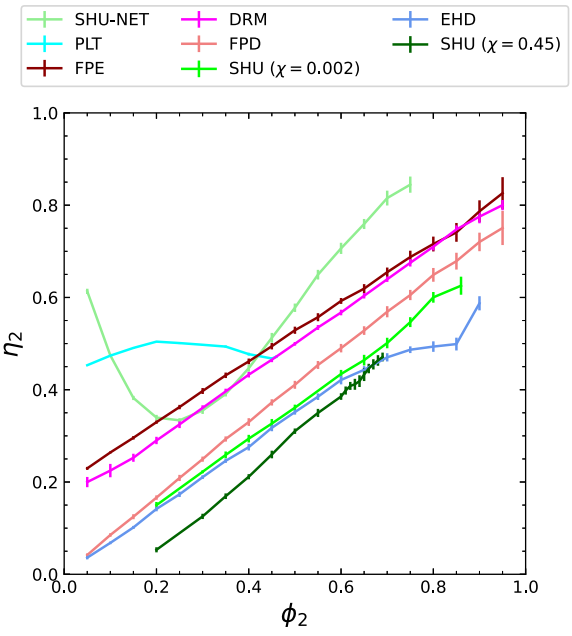


Fig. 2. Plots of the three-point parameter ζ_2 as a function of phase 2 volume fraction ϕ_2 for the (a) 2D and (b) 3D systems, computed using the Monte Carlo integration algorithm described in Section 4. The abbreviations for the models listed in the legend are defined in Table 1. The error bars represent the standard deviation of ζ_2 for an ensemble of configurations at a given value of ϕ_2.

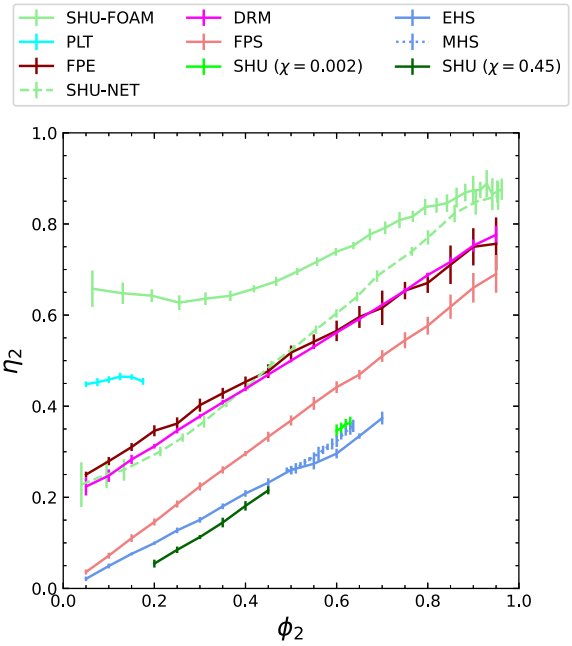
5.2. Comparison of the various approximations to simulated results

In this subsection, we use our calculated values of ζ_2 and η_2 in the various three-point approximations described in Section 2.3 as well as numerical simulations to compare and contrast the effective conductivities σ_e and the bulk K_e and shear G_e moduli of some of the model microstructures considered in this paper. Note that effective properties for the fully penetrable disk and ellipse models were obtained numerically using finite element methods in COMSOL Multiphysics®. Those for the fully penetrable sphere and ellipsoid systems, as well as the 2D and 3D Debye random media and hard platelet systems were obtained using the Fast Fourier Transform (FFT)-based homogenization solver

[6] Mathematically, this behavior is attributable to the factors of $\cos(4\theta)$ and $P_4(\cos\theta)$ in integrals (28) and (29), respectively, which have a greater smoothing effect on the integrand than do the $\cos(2\theta)$ and $P_2(\cos\theta)$ terms in the corresponding ζ_2 integrals.



(a)



(b)

Fig. 3. Plots of the three-point parameter η_2 as a function of phase 2 volume fraction ϕ_2 for the (a) 2D and (b) 3D systems, computed using the Monte Carlo integration algorithm described in Section 4. The abbreviations for the models listed in the legend are defined in Table 1. The error bars represent the standard deviation of η_2 for an ensemble of configurations at a given value of ϕ_2.

described in Ref. [176]. All numerical values of σ_e, K_e, and G_e obtained via the aforementioned simulations are tabulated in the Supporting Information.

Overall, the structurally diverse disordered 2D and 3D models considered in this section exhibit effective conductivities and elastic moduli that nearly span the Hashin–Shtrikman bounds and are generally rank-ordered for a given ϕ_2 according to their values of ζ_2 and η_2, as seen in the plots of σ_e vs. ϕ_2 in Fig. 4, K_e vs. ϕ_2 in Fig. 5, and G_e vs. ϕ_2 in Fig. 6. Such behavior is expected for these models as their geometrical and topological features span between those of extremal structures. For a given ϕ_2 among the models considered here, the three-point approximations (16), (25), and (26) (with phase 1 as the connected phase) respectively predict that σ_e, K_e, and G_e are the closest to the HS lower bounds for the $\chi = 0.45$ stealthy hyperuniform disk and sphere packings, equilibrium hard disk, and metastable hard spheres, while (16) and (25) (with phase 2 as the connected phase) respectively predict that σ_e and K_e are the closest to the HS upper bounds for the 2D networks and 3D foams. While (26) predicts that the 3D foams have G_e close to the HS upper bound for virtually all ϕ_2, it predicts that the shear moduli of the 2D networks are not appreciably close to the HS upper bound for any ϕ_2. This behavior is expected as networks with similar honeycomb structures have been shown to have non-optimal G_e due to certain structural bending modes [51,119,174,175].

Otherwise, it is seen through both simulated data and various approximations that the fully penetrable particle models, as well as the 2D and 3D hard platelet and Debye random media systems all have σ_e, K_e, and G_e that are intermediate to the Hashin–Shtrikman bounds in Figs. 4–6. We also see good overall agreement in these plots between the various approximations and simulated data, with the small $(1-5\%)$ discrepancies being attributable to a combination of the limitations on the values of ζ_2 and η_2 in the approximations discussed in Section 2.3, as well as digitization errors in the simulations that are discussed in the Supporting Information. Finally, we observe that the overall spread of effective elastic moduli of the 2D and 3D models is generally smaller than that of the effective conductivities in both 2D and 3D. Such narrower spreads of K_e and G_e relative to that of σ_e was also observed by Gillman et al. in disordered packings of platonic solids [76].

6. Conclusions

In summary, we have shown through comprehensive numerical calculations that the three-point parameters ζ_2 and η_2 of a wide-variety of disordered 2D and 3D model microstructures tend to be larger for those in which phase 2 is more well-connected and phase 1 is more disconnected for a given a volume fraction. This computationally challenging task was accomplished using our efficient and accurate Monte Carlo algorithm. Through rigorous approximation formulas that incorporate ζ_2 and η_2 as well as numerical simulations, we show that our models have σ_e, K_e, and G_e that nearly span the Hashin–Shtrikman bounds across volume fractions due to the choice of model microstructures that we have examined, which span a wide spectrum of phase geometries and topologies with varying degrees of disorder. Of note are the disordered $\chi = 0.45$ stealthy disk and sphere packings, as well as the disordered 2D networks and 3D foams which have nearly extremal effective conductivities and bulk moduli across volume fractions. With the exception of the 2D networks, these models also have nearly extremal shear moduli. We note that one could likely generate disordered *triangular* honeycomb-like networks with nearly optimal σ_e, K_e, *and* G_e across volume fractions using Delaunay-triangulations of stealthy hyperuniform point patterns for reasons discussed in Refs. [51,119].

While all of the simulated models considered here were under periodic boundary conditions, our Monte Carlo integration algorithm can also be used to ascertain ζ_2 and η_2 for material microstructures obtained via experimental methods (i.e., microscopy or tomography techniques). In these cases, one must simply ensure that the triangles used to sample the indicator function $\mathcal{I}(\mathbf{r})$ in summation (44) do not intersect the sample boundaries. Our Monte Carlo integration scheme can also be adapted to efficiently compute certain integrals over S_3 that arise in rigorous approximations of *frequency-dependent dynamic* dielectric constants and elastic moduli [18,20], potentially bypassing the need for computationally-costly finite-element simulations.

Using inverse methods and our Monte Carlo integration algorithm, one could computationally design disordered microstructures with optimal σ_e, K_e, and G_e by targeting those with $\zeta_2 = 1$ and $\eta_2 = 1$.

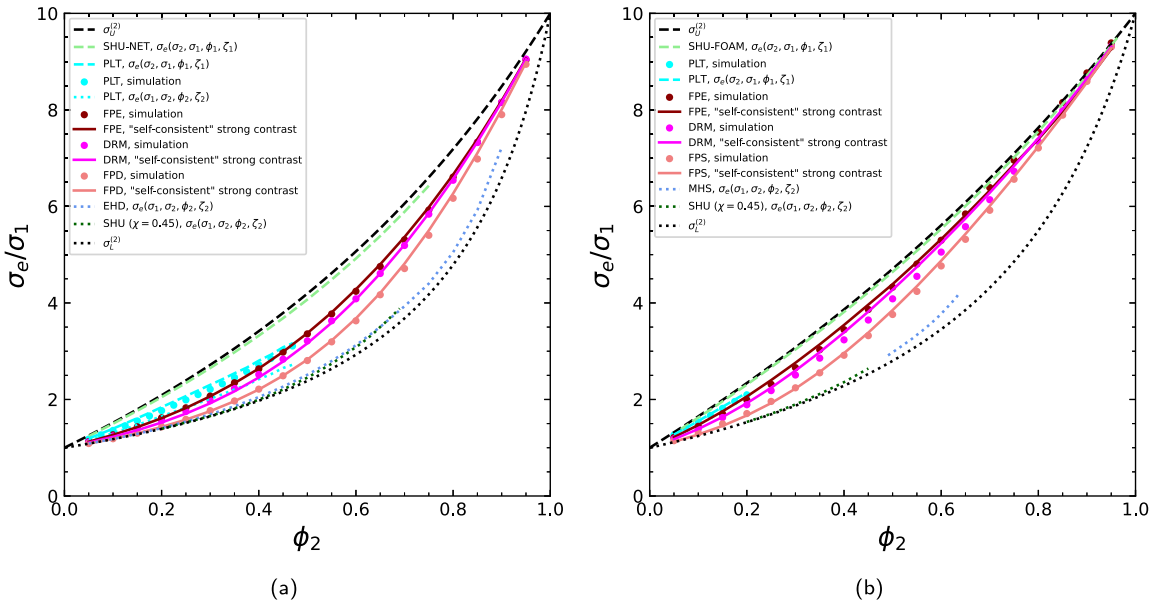


Fig. 4. Plots of the scaled effective conductivity σ_e/σ_1 as a function of phase 2 volume fraction ϕ_2 for various microstructures in (a) 2D and (b) 3D. In both plots (a) and (b), the dotted and dashed black lines respectively correspond to the Hashin–Shtrikman lower and upper bounds on the effective conductivity (22) and (23), the scatter plots correspond to values of σ_e obtained via numerical methods, the dotted and dashed lines correspond to the three-point approximation (16) in which phase 2 is taken to be the dispersed and matrix phase, respectively, and the solid lines correspond to the "self-consistent" strong contrast approximation (19). For all results in (a) and (b), the phase conductivity contrast ratio is $\sigma_2/\sigma_1 = 10$.

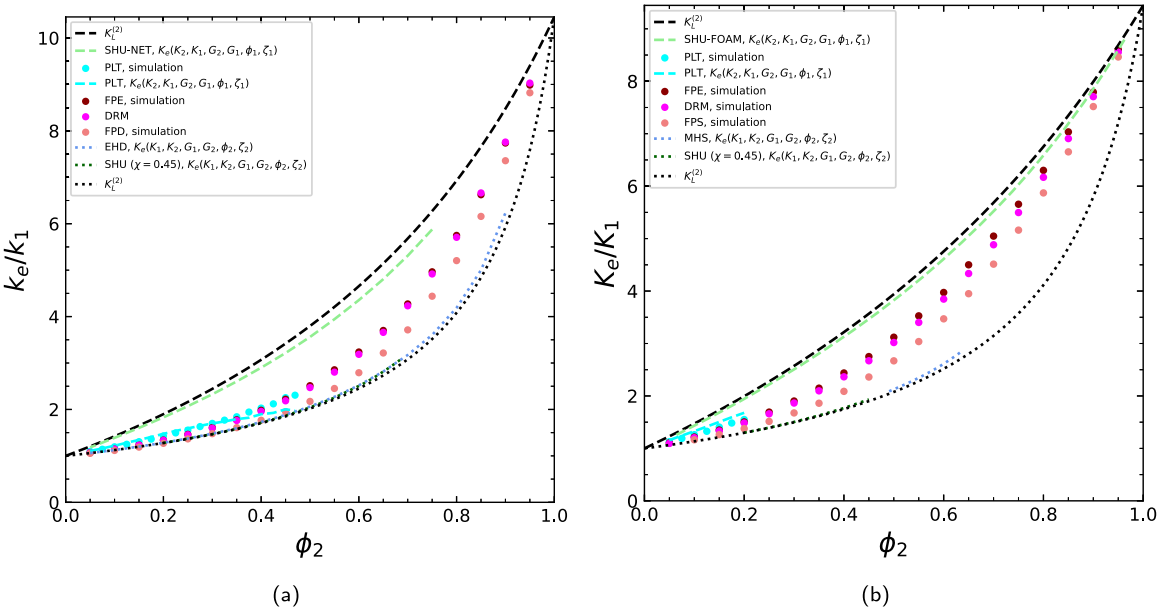


Fig. 5. Plots of the scaled effective bulk moduli K_e/K_1 as a function of phase 2 volume fraction ϕ_2 for various microstructures in (a) 2D and (b) 3D. Note that for the 2D models in (a), we consider plane-strain conditions and denote the bulk modulus as k_e. In both plots (a) and (b), the dotted and dashed black lines respectively correspond to the Hashin–Shtrikman lower and upper bounds on K_e (36) and (37), the scatter plots correspond to values of K_e obtained via numerical methods, and the dotted and dashed lines correspond to the three-point approximation (25) in which phase 2 is taken to be the dispersed and matrix phase, respectively. For these results, the phase contrast ratios for the 2D and 3D bulk moduli are $k_2/k_1 \approx 10.45$ and $K_2/K_1 \approx 9.45$, respectively. The phase contrast ratio for the shear moduli is $G_2/G_1 \approx 19.5$. Note that only simulated values of the bulk moduli for Debye random media and the fully penetrable particle models are shown in (a) and (b) as (25) is not applicable to systems with such large clusters of phase 2.

Specifically, some initial structure could be stochastically evolved via perturbations to the microstructure (e.g., pixel and voxel swap moves) until the target three-point parameters are achieved using simulated annealing. Via its use of stratified sampling, our Monte Carlo integration scheme makes it possible to efficiently update the values of ζ_2 and η_2 by only resampling the contributions to (44) in the strata that are affected by each pixel/voxel swap. Note that the aforementioned algorithm is an adaptation of the Yeong-Torquato stochastic microstructure reconstruction method [13] in which specific values of ζ_2 and η_2 are targeted in the objective function rather than or in addition to correlation functions like the autocovariance. The 3D foams considered here are potentially desirable initial conditions for this optimization scheme

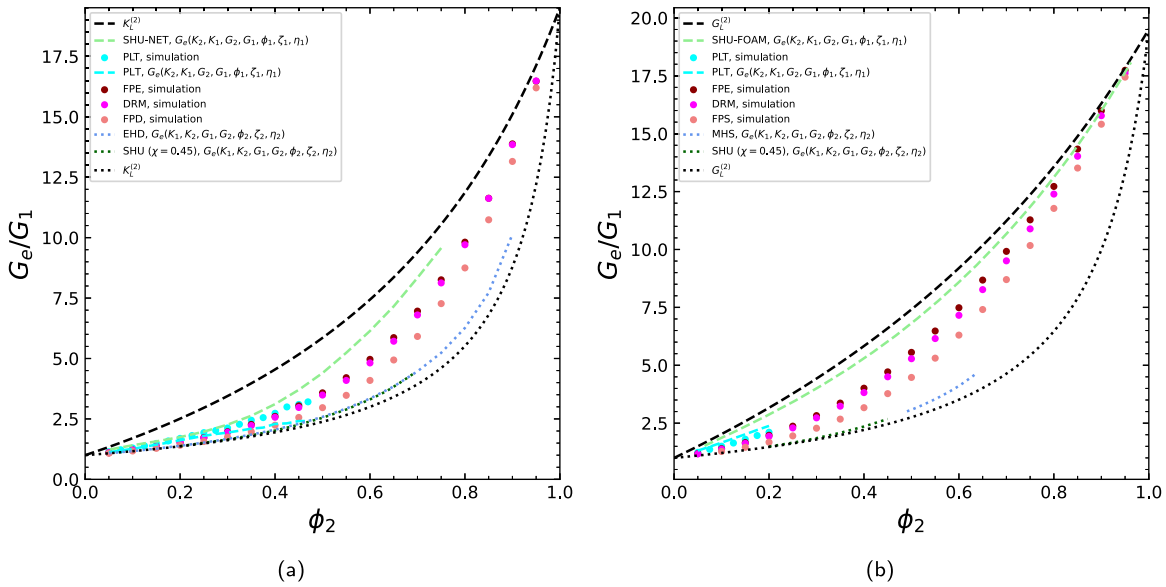


Fig. 6. Plots of the scaled effective shear moduli G_e/G_1 as a function of phase 2 volume fraction ϕ_2 for various microstructures in (a) 2D and (b) 3D. Note that for the 2D models in (a), we consider plane-strain conditions. In both plots (a) and (b), the dotted and dashed black lines respectively correspond to the Hashin–Shtrikman lower and upper bounds on G_e (38) and (39), the scatter plots correspond to values of G_e obtained via numerical methods, and the dotted and dashed lines correspond to the three-point approximation (26) in which phase 2 is taken to be the dispersed and matrix phase, respectively. For these results, the phase contrast ratios for the 2D and 3D bulk moduli are $k_2/k_1 \approx 10.45$ and $K_2/K_1 \approx 9.45$, respectively. The phase contrast ratio for the shear moduli is $G_2/G_1 \approx 19.5$. Note that only simulated values of the shear moduli for Debye random media and the fully penetrable particle models are shown in (a) and (b) as (26) is not applicable to systems with such large clusters of phase 2.

as they already have ζ_2 and η_2 close to unity. Moreover, by placing certain constraints [177] on the wall topology to ensure that these structures remain self-supporting during the procedure, the resulting optimal disordered microstructures could be manufactured using 3D printing techniques [178].

CRediT authorship contribution statement

M. Skolnick: Writing – original draft, Validation, Software, Methodology, Investigation, Formal analysis, Conceptualization. **S. Torquato:** Writing – original draft, Validation, Supervision, Methodology, Funding acquisition, Formal analysis, Conceptualization.

Acknowledgments

This work was sponsored by the Army Research Office, United States and was accomplished under Cooperative Agreement Number W911NF-22-2-0103, as well as the Air Force Office of Scientific Research Program under award No. FA9550-18-1-0514. M.S. also acknowledges the support of the Harold W. Dodds Honorific Fellowship. M.S. thanks Dr. Charles Maher for helpful discussions, and Dr. Jaeuk Kim for helpful discussions and providing the stealthy hyperuniform disk and sphere configurations. The authors thank the Princeton Institute for Computational Science and Engineering (PICSciE) for the computational resources.

Declaration of competing interest

The authors declare that they have no known competing financial interests or personal relationships that could have appeared to influence the work reported in this paper.

Appendix A. Supplementary data

Supplementary material related to this article can be found online at https://doi.org/10.1016/j.actamat.2025.120921.

References

[1] S. Torquato, Random Heterogeneous Materials: Microstructure and Macroscopic Properties, Springer-Verlag, New York, 2002.
[2] M. Sahimi, Heterogeneous Materials I: Linear Transport and Optical Properties, Springer-Verlag, New York, 2003.
[3] G.W. Milton, The Theory of Composites, Cambridge University Press, Cambridge, England, 2002.
[4] B. Patel, T.I. Zohdi, Numerical estimation of effective electromagnetic properties for design of particulate composites, Mater. Des. 94 (2016) 546–553.
[5] S. Torquato, Morphology and effective properties of disordered heterogeneous media, Int. J. Solids Struct. 35 (1998) 2385.
[6] A. Chremos, J.F. Douglas, Particle localization and hyperuniformity of polymer-grafted nanoparticle materials, Ann. Phys., Lpz. 529 (5) (2017) 1600342.
[7] A. Chremos, J.F. Douglas, Hidden hyperuniformity in soft polymeric materials, Phys. Rev. Lett. 121 (2018) 258002.
[8] M. Huang, W. Hu, S. Yang, Q.-X. Liu, H. Zhang, Circular swimming motility and disordered hyperuniform state in an algae system, Proc. Natl. Acad. Sci. 118 (18) (2021) e2100493118.
[9] S. Torquato, M. Skolnick, J. Kim, Local order metrics for two-phase media across length scales, J. Phys. A: Math. Theor. 55 (27) (2022) 274003.
[10] S. Torquato, J. Kim, Novel equilibrium route toward nonequilibrium jammed hard-sphere hyperuniform glasses, 2024, preprint.
[11] J. Kim, S. Torquato, Dense sphere packings derived from disordered stealthy hyperuniform ground states, 2024, preprint.
[12] P. Debye, H.R. Anderson, H. Brumberger, Scattering by an inhomogeneous solid. II. The correlation function and its applications, J. Appl. Phys. 28 (1957) 679–683.
[13] C.L.Y. Yeong, S. Torquato, Reconstructing random media, Phys. Rev. E 57 (1998) 495–506.
[14] Z. Ma, S. Torquato, Generation and structural characterization of Debye random media, Phys. Rev. E 102 (2020) 043310.
[15] M. Skolnick, S. Torquato, Understanding degeneracy of two-point correlation functions via debye random media, Phys. Rev. E 104 (2021) 045306.
[16] M. Florescu, S. Torquato, P.J. Steinhardt, Designer disordered materials with large complete photonic band gaps, Proc. Nat. Acad. Sci. 106 (2009) 20658–20663.
[17] S. Kamrava, P. Tahmasebi, M. Sahimi, Linking morphology of porous media to their macroscopic permeability by deep learning, Transp. Porous Media 131 (2019) 427–448.
[18] J. Kim, S. Torquato, Effective elastic wave characteristics of composite media, New J. Phys. 22 (2020) 123050.
[19] J. Kim, S. Torquato, Multifunctional composites for elastic and electromagnetic wave propagation, Proc. Nat. Acad. Sci. 117 (2020) 8764–8774.

[20] S. Torquato, J. Kim, Nonlocal effective electromagnetic wave characteristics of composite media: Beyond the quasistatic regime, Phys. Rev. X 11 (2021) 021002.

[21] M. Sahimi, P. Tahmasebi, Reconstruction, optimization, and design of heterogeneous materials and media: Basic principles, computational algorithms, and applications, Phys. Rep. 939 (2021) 1–82.

[22] A.K. Sen, S. Torquato, Effective conductivity of anisotropic two-phase composite media, Phys. Rev. B 39 (1989) 4504–4515.

[23] S. Torquato, Exact expression for the effective elastic tensor of disordered composites, Phys. Rev. Lett. 79 (1997) 681–684.

[24] S. Torquato, Microscopic Approach to Transport in Two-Phase Random Media (Ph.D. thesis), State University of New York at Stony Brook, 1981.

[25] G.W. Milton, Bounds on the transport and optical properties of a two-component composite material, J. Appl. Phys. 52 (1981) 5294–5304.

[26] G.W. Milton, Bounds on the electromagnetic, elastic, and other properties of two-component composites, Phys. Rev. Lett. 46 (1981) 542–545.

[27] G.W. Milton, Bounds on the elastic and transport properties of two-component composites, J. Mech. Phys. Solids 30 (1982) 177–191.

[28] S. Torquato, Effective electrical conductivity of two-phase disordered composite media, J. Appl. Phys. 58 (1985) 3790–3797.

[29] S. Torquato, J. Kim, Microstructural and transport characteristics of triply periodic bicontinuous materials, Acta Mater. 276 (2024) 120142.

[30] S. Torquato, Effective stiffness tensor of composite media: I. Exact series expansions, J. Mech. Phys. Solids 45 (1997) 1421–1448.

[31] S. Torquato, Effective stiffness tensor of composite media: II. Applications to isotropic dispersions, J. Mech. Phys. Solids 46 (1998) 1411–1440.

[32] S. Torquato, Predicting transport characteristics of hyperuniform porous media via rigorous microstructure–property relations, Adv. Water Resour. 140 (2020) 103565.

[33] M.A. Klatt, R.M. Ziff, S. Torquato, Critical pore radius and transport properties of disordered hard-and overlapping-sphere models, Phys. Rev. E 104 (2021) 014127.

[34] M.J. Beran, J. Molyneux, Use of classical variational principles to determine bounds for the effective bulk modulus in heterogeneous media, Quart. Appl. Math. 24 (1966) 107–118.

[35] J.J. McCoy, On the displacement field in an elastic medium with random variation of material properties, in: Recent Advances in Engineering Sciences, Vol. 5, Gordon and Breach, New York, 1970.

[36] N. Silnutzer, Effective Constants of Statistically Homogeneous Materials (Ph.D. thesis), University of Pennsylvania, Philadephia, 1972.

[37] K. Schulgasser, On the conductivity of fiber reinforced materials, J. Math. Phys. 17 (1976) 382–387.

[38] G.W. Milton, N. Phan-Thien, New bounds on effective elastic moduli of two-component materials, Proc. R. Soc. Lond. A 380 (1982) 305–331.

[39] N. Phan-Thien, G.W. Milton, New bounds on the effective thermal conductivity of n-phase materials, Proc. R. Soc. Lond. A 380 (1982) 333–348.

[40] G.W. Milton, Correlation of the electromagnetic and elastic properties of composites and microgeometries corresponding with effective medium approximations, in: D.L. Johnson, P.N. Sen (Eds.), Physics and Chemistry of Porous Media, AIP, New York, 1984.

[41] L.V. Gibiansky, S. Torquato, Geometrical-parameter bounds on effective moduli of composites, J. Mech. Phys. Solids 43 (1995) 1587–1613.

[42] L.V. Gibiansky, S. Torquato, Rigorous link between the conductivity and elastic moduli of fibre-reinforced composite materials, Phil. Trans. R. Soc. Lond. A. 353 (1995) 243–278.

[43] Z. Hashin, S. Shtrikman, A variational approach to the theory of the effective magnetic permeability of multiphase materials, J. Appl. Phys. 33 (1962) 3125–3131.

[44] Z. Hashin, S. Shtrikman, A variational approach to the elastic behavior of multiphase materials, J. Mech. Phys. Solids 4 (1963) 286–295.

[45] Z. Hashin, On elastic behavior of fiber reinforced materials of arbitrary transverse phase geometry, J. Mech. Phys. Solids 13 (1965) 119–134.

[46] Z. Hashin, Theory of composite materials, in: Mechanics of Composite Materials, Pergamon Press, New York, 1970.

[47] R.C. McPhedran, G.W. Milton, Bounds and exact theories for the transport properties of inhomogeneous media, Appl. Phys. A 26 (1981) 207–220.

[48] J.W. Eischen, S. Torquato, Determining elastic behavior of composites by the boundary element method, J. Appl. Phys. 74 (1993) 159–170.

[49] J. Helsing, Bounds on the shear modulus of composites by interface integral methods, J. Mech. Phys. Solids 42 (1994) 1123–1138.

[50] M. Röding, Effective diffusivity in lattices of impermeable superballs, Phys. Rev. E 98 (2018) 052908.

[51] S. Hyun, S. Torquato, Effective elastic and transport properties of regular honeycombs for all densities, J. Mater. Res. 15 (2000) 1985–1993.

[52] S. Torquato, S. Hyun, Effective-medium approximation for composite media: Realizable single-scale dispersions, J. Appl. Phys. 89 (2001) 1725–1729.

[53] S. Torquato, J.D. Beasley, Effective properties of fiber-reinforced materials: I. Bounds on the effective thermal conductivity of dispersions of fully penetrable cylinders, Internat. J. Engrg. Sci. 24 (1986) 415–433.

[54] S. Torquato, J.D. Beasley, Effective properties of fiber-reinforced materials: II. Bounds on the effective elastic moduli of dispersions of fully penetrable cylinders, Internat. J. Engrg. Sci. 24 (1986) 435–447.

[55] S. Torquato, G. Stell, J. Beasley, Third-order bounds on the effective bulk and shear moduli of a dispersion of fully penetrable spheres, Internat. J. Engrg. Sci. 23 (1985) 385–392.

[56] J.G. Berryman, Variational bounds on elastic constants for the penetrable sphere model, J. Phys. D 18 (1985) 585–597.

[57] A.P. Roberts, E.J. Garboczi, Computation of the linear elastic properties of random porous materials with a wide variety of microstructure, Proc. R. Soc. Lond. A 458 (2002) 1033–1054.

[58] A.P. Roberts, M.A. Knackstedt, Structure-property correlations in model composite materials, Phys. Rev. E 54 (1996) 2313–2328.

[59] S. Torquato, F. Lado, Bounds on the conductivity of a random array of cylinders, Proc. R. Soc. Lond. A 417 (1988) 59–80.

[60] S. Torquato, F. Lado, Bounds on the effective transport and elastic properties of cylindrical fibers in a matrix, J. Appl. Mech. 55 (1988) 347–354.

[61] C.A. Miller, S. Torquato, Improved bounds on elastic and transport properties of fiber-reinforced composites: Effect of polydispersivity in fiber radius, J. Appl. Phys. 69 (1991) 1948–1955.

[62] L. Greengard, J. Helsing, A numerical study of the ζ_2 parameter for random suspensions of disks, J. Appl. Phys. 77 (1995) 2015–2019.

[63] S. Torquato, F. Lado, Effective properties of two-phase disordered composite media. II. Evaluation of bounds on the conductivity and bulk modulus of dispersions of impenetrable spheres, Phys. Rev. B 33 (1986) 6428–6435.

[64] S. Torquato, F. Lado, P.A. Smith, Bulk properties of two-phase disordered media: IV. Mechanical properties of suspensions of penetrable spheres at nondilute concentrations, J. Chem. Phys. 86 (1987) 6388–6393.

[65] C.A. Miller, S. Torquato, Effective conductivity of hard sphere dispersions, J. Appl. Phys. 68 (1990) 5486–5493.

[66] J.F. Thovert, I.C. Kim, S. Torquato, A. Acrivos, Bounds on the effective properties of polydispersed suspensions of spheres: An evaluation of two relevant morphological parameters, J. Appl. Phys. 67 (1990) 6088–6098.

[67] M.N. Miller, Bounds for effective electrical, thermal, and magnetic properties of heterogeneous materials, J. Math. Phys. 10 (1969) 1988–2004.

[68] M.J. Beran, N.R. Silnutzer, Effective electrical, thermal and magnetic properties of fiber reinforced materials, J. Compos. Mater. 5 (1971) 246–249.

[69] J. Helsing, Third-order bounds on the conductivity of a random stacking of cubes, J. Math. Phys. 35 (1994) 1688–1692.

[70] J.H. Hetherington, M.F. Thorpe, The conductivity of a sheet containing inclusions with sharp corners, Proc. R. Soc. Lond. A 438 (1992) 591–604.

[71] A.P. Roberts, M. Teubner, Transport properties of heterogeneous materials derived from Gaussian random fields: Bounds and simulation, Phys. Rev. E 51 (1995) 4141–4154.

[72] F. Gritti, G. Guiochon, Diffusion models in chromatographic columns packed with fully and superficially porous particles, Chem. Eng. Sci. 66 (17) (2011) 3773–3781.

[73] F. Gritti, G. Guiochon, Theoretical investigation of diffusion along columns packed with fully and superficially porous particles, J. Chromatogr. A 1218 (22) (2011) 3476–3488.

[74] G. Desmet, K. Broeckhoven, S. Deridder, D. Cabooter, Review of recent insights in the measurement and modelling of the b-term dispersion and related mass transfer properties in liquid chromatography, Anal. Chim. Acta 1214 (2022) 339955.

[75] A. Gillman, K. Matouš, Third-order model of thermal conductivity for random polydisperse particulate materials using well-resolved statistical descriptions from tomography, Phys. Lett. A 378 (2014) 3070–3073.

[76] A. Gillman, G. Amadio, K. Matouš, T.L. Jackson, Third-order thermo-mechanical properties for packs of platonic solids using statistical micromechanics, Proc. R. Soc. Lond. A: Math. Phys. Eng. Sci. 471 (2015) 20150060.

[77] P.B. Corson, Correlation functions for predicting properties of heterogeneous materials. III. Effective elastic moduli of two-phase solids, J. Appl. Phys. 45 (1974) 3171–3179.

[78] P.B. Corson, Correlation functions for predicting properties of heterogeneous materials. IV. Effective thermal conductivity of two-phase solids, J. Appl. Phys. 45 (1974) 3180–3182.

[79] D.A. Coker, S. Torquato, J.H. Dunsmuir, Morphology and physical properties of Fontainebleau sandstone via a tomographic analysis, J. Geophys. Res. 101 (1996) 17497–17506.

[80] S. Torquato, C.L.Y. Yeong, M.D. Rintoul, D.L. Milius, I.A. Aksay, Elastic properties and structure of interpenetrating boron carbide aluminum multiphase composites, J. Am. Ceram. Soc. 82 (1999) 1263–1268.

[81] H. Li, S. Singh, C. Shashank Kaira, J.C. Mertens, J.J. Williams, N. Chawla, Y. Jiao, Microstructural quantification and property prediction using limited X-ray tomography data, JOM 68 (8) (2016) 2288–2295.

[82] S. Torquato, G. Stell, Microstructure of two-phase random media: V. The n-point matrix probability functions for impenetrable spheres, J. Chem. Phys. 82 (1985) 980–987.

[83] S. Torquato, G. Stell, Bounds on the effective thermal conductivity of a dispersion of fully penetrable spheres, Internat. J. Engrg. Sci. 23 (1985) 375–383.

[84] S. Torquato, Bulk properties of two-phase disordered media: II. Effective conductivity of a dilute dispersion of penetrable spheres, J. Chem. Phys. 83 (1985) 4776–4785.
[85] P.A. Smith, S. Torquato, Computer simulation results for bounds on the effective conductivity of composite media, J. Appl. Phys. 65 (1989) 893–900.
[86] H. Malmir, M. Sahimi, Y. Jiao, Higher-order correlation functions in disordered media: Computational algorithms and application to two-phase heterogeneous materials, Phys. Rev. E 98 (2018) 063317.
[87] D. Hlushkou, H. Liasneuski, U. Tallarek, S. Torquato, Effective diffusion coefficients in random packings of polydisperse hard spheres from two-point and three-point correlation functions, J. Appl. Phys. 118 (2015) 124901.
[88] S. Torquato, G. Stell, Microstructure of two-phase random media: I. The *n*-point probability functions, J. Chem. Phys. 77 (1982) 2071–2077.
[89] S. Torquato, G. Stell, Microstructure of two-phase random media: II. The Mayer–Montroll and Kirkwood–Salsburg hierarchies, J. Chem. Phys. 78 (1983) 3262–3272.
[90] S. Torquato, P. Smith, Latent heat of vaporization of a widely diverse class of fluids, J. Heat Transf. 106 (1984) 252.
[91] S. Torquato, F.H. Stillinger, Local density fluctuations, hyperuniform systems, and order metrics, Phys. Rev. E 68 (2003) 041113.
[92] C.E. Zachary, S. Torquato, Hyperuniformity in point patterns and two-phase heterogeneous media, J. Stat. Mech.: Theory Exp. 2009 (2009) P12015.
[93] S. Torquato, Hyperuniformity and its generalizations, Phys. Rev. E 94 (2016) 022122.
[94] S. Torquato, Hyperuniform states of matter, Phys. Rep. 745 (2018) 1–95.
[95] S. Torquato, Disordered hyperuniform heterogeneous materials, J. Phys.: Condens. Matter. 28 (2016) 414012.
[96] W. Man, M. Florescu, K. Matsuyama, P. Yadak, G. Nahal, S. Hashemizad, E. Williamson, P. Steinhardt, S. Torquato, P. Chaikin, Photonic band gap in isotropic hyperuniform disordered solids with low dielectric contrast, Opt. Express 21 (2013) 19972–19981.
[97] G. Gkantzounis, T. Amoah, M. Florescu, Hyperuniform disordered phononic structures, Phys. Rev. B 95 (2017) 094120.
[98] S. Yu, C.-W. Qiu, Y. Chong, S. Torquato, N. Park, Engineered disorder in photonics, Nat. Rev. Mater. 6 (2021) 226–243.
[99] M. Klatt, P. Steinhardt, S. Torquato, Wave propagation and band tails of two-dimensional disordered systems in the thermodynamic limit, Proc. Natl. Acad. Sci. 119 (52) (2022) e2213633119.
[100] Y. Jiao, T. Lau, H. Hatzikirou, M. Meyer-Hermann, J.C. Corbo, S. Torquato, Avian photoreceptor patterns represent a disordered hyperuniform solution to a multiscale packing problem, Phys. Rev. E 89 (2014) 022721.
[101] R. Degl'Innocenti, Y.D. Shah, L. Masini, A. Ronzani, A. Pitanti, Y. Ren, D.S. Jessop, A. Tredicucci, H.E. Beere, D.A. Ritchie, Hyperuniform disordered terahertz quantum cascade laser, Sci. Rep. 6 (2016) 19325.
[102] W. Zhou, Z. Cheng, B. Zhu, X. Sun, H.K. Tsang, Hyperuniform disordered network polarizers, IEEE J. Sel. Top. Quantum Elec. 22 (2016) 288–294.
[103] F. Bigourdan, R. Pierrat, R. Carminati, Enhanced absorption of waves in stealth hyperuniform disordered media, Opt. Express 27 (2019) 8666–8682.
[104] S. Gorsky, W.A. Britton, Y. Chen, J. Montaner, A. Lenef, M. Raukas, L. Dal Negro, Engineered hyperuniformity for directional light extraction, APL Photonics 4 (2019) 110801.
[105] A. Sheremet, R. Pierrat, R. Carminati, Absorption of scalar waves in correlated disordered media and its maximization using stealth hyperuniformity, Phys. Rev. A 101 (2020) 053829.
[106] R. Lin, V. Mazzone, N. Alfaraj, J. Liu, X. Li, A. Fratalocchi, On-chip hyperuniform lasers for controllable transitions in disordered systems, Laser Photonics Rev. 14 (2) (2020) 1800296.
[107] D. Chen, X. Jiang, D. Wang, J. Vidallon, H. Zhuang, Y. Jiao, Multihyperuniform long-range order in medium-entropy alloys, Acta Mater. 246 (2023) 118678.
[108] G. Zhang, F.H. Stillinger, S. Torquato, Transport, geometrical and topological properties of stealthy disordered hyperuniform two-phase systems, J. Chem. Phys. 145 (2016) 244109.
[109] D. Chen, S. Torquato, Designing disordered hyperuniform two-phase materials with novel physical properties, Acta Mater. 142 (2018) 152–161.
[110] Y. Xu, S. Chen, P.-E. Chen, W. Xu, Y. Jiao, Microstructure and mechanical properties of hyperuniform heterogeneous materials, Phys. Rev. E 96 (2017) 043301.
[111] O. Leseur, R. Pierrat, R. Carminati, High-density hyperuniform materials can be transparent, Optica 3 (2016) 763–767.
[112] L.S. Froufe-Pérez, M. Engel, J. José Sáenz, F. Scheffold, Transport phase diagram and Anderson localization in hyperuniform disordered photonic materials, Proc. Nat. Acad. Sci. 114 (2017) 9570–9574.
[113] L.S. Froufe-Pérez, G.J. Aubry, F. Scheffold, S. Magkiriadou, Bandgap fluctuations and robustness in two-dimensional hyperuniform dielectric materials, Opt. Express 31 (11) (2023) 18509–18515.
[114] J. Kim, S. Torquato, Effective electromagnetic wave properties of disordered stealthy hyperuniform layered media beyond the quasistatic regime, Optica 10 (8) (2023) 965–972.
[115] J. Kim, S. Torquato, Theoretical prediction of the effective dynamic dielectric constant of disordered hyperuniform anisotropic composites beyond the long-wavelength regime, Opt. Mater. Express 14 (1) (2024) 194–215.
[116] J. Kim, S. Torquato, Extraordinary optical and transport properties of disordered stealthy hyperuniform two-phase media, J. Phys.: Condens. Matter. 36 (22) (2024) 225701.
[117] Y. Zheng, L. Liu, H. Nan, Z.-X. Shen, G. Zhang, D. Chen, L. He, W. Xu, M. Chen, Y. Jiao, H. Zhuang, Disordered hyperuniformity in two-dimensional amorphous silica, Sci. Adv. 6 (2020) eaba0826.
[118] D. Chen, Y. Zheng, L. Liu, G. Zhang, M. Chen, Y. Jiao, H. Zhuang, Stone–wales defects preserve hyperuniformity in amorphous two-dimensional networks, Proc. Natl. Acad. Sci. 118 (2021) e2016862118.
[119] S. Torquato, D. Chen, Multifunctional hyperuniform cellular networks: optimality, anisotropy and disorder, Multifunct. Mater. 1 (2018) 015001.
[120] M. Florescu, S. Torquato, P.J. Steinhardt, Complete band gaps in two-dimensional photonic quasicrystals, Phys. Rev. B 80 (2009) 155112.
[121] C. De Rosa, F. Auriemma, C. Diletto, R. Di Girolamo, A. Malafronte, P. Morvillo, G. Zito, G. Rusciano, G. Pesce, A. Sasso, Toward hyperuniform disordered plasmonic nanostructures for reproducible surface-enhanced Raman spectroscopy, Phys. Chem. Chem. Phys. 17 (2015) 8061–8069.
[122] T. Ma, H. Guerboukha, M. Girard, A.D. Squires, R.A. Lewis, M. Skorobogatiy, 3D printed hollow-core terahertz optical waveguides with hyperuniform disordered dielectric reflectors, Adv. Opt. Mater. 4 (2016) 2085–2094.
[123] A. Chremos, J.F. Douglas, Particle localization and hyperuniformity of polymer-grafted nanoparticle materials, Ann. Phys., Lpz. 529 (2017).
[124] H. Zhang, H. Chu, H. Giddens, W. Wu, Y. Hao, Experimental demonstration of luneburg lens based on hyperuniform disordered media, Appl. Phys. Lett. 114 (2019) 053507.
[125] W. Wu, M. Singh, A. Masud, X. Wang, A. Nallapaneni, Z. Xiao, Y. Zhai, Z. Wang, T. Terlier, M. Bleuel, G. Yuan, S.K. Satija, J.F. Douglas, K. Matyjaszewski, M.R. Bockstaller, A. Karim, Control of phase morphology of binary polymer grafted nanoparticle blend films via direct immersion annealing, ACS Nano 15 (7) (2021) 12042–12056.
[126] F. Sgrignuoli, L. Dal Negro, Hyperuniformity and wave localization in pinwheel scattering arrays, Phys. Rev. B 103 (2021) 224202.
[127] F. Sgrignuoli, S. Torquato, L. Dal Negro, Subdiffusive wave transport and weak localization transition in three-dimensional stealthy hyperuniform disordered systems, Phys. Rev. B 105 (2022) 064204.
[128] A. Rohfritsch, J.-M. Conoir, T. Valier-Brasier, R. Marchiano, Impact of particle size and multiple scattering on the propagation of waves in stealthy-hyperuniform media, Phys. Rev. E 102 (2020) 053001.
[129] H. Zhang, Q. Cheng, H. Chu, O. Christogeorgos, W. Wu, Y. Hao, Hyperuniform disordered distribution metasurface for scattering reduction, Appl. Phys. Lett. 118 (2021) 101601.
[130] Y. Zheng, D. Chen, L. Liu, Y. Liu, M. Chen, H. Zhuang, Y. Jiao, Topological transformations in hyperuniform pentagonal two-dimensional materials induced by stone-wales defects, Phys. Rev. B 103 (2021) 245413.
[131] D. Chen, Y. Zheng, C.-H. Lee, S. Kang, W. Zhu, H. Zhuang, P. Huang, Y. Jiao, Nearly hyperuniform, nonhyperuniform, and antihyperuniform density fluctuations in two-dimensional transition metal dichalcogenides with defects, Phys. Rev. B 103 (2021) 224102.
[132] N. Granchi, R. Spalding, M. Lodde, M. Petruzzella, F. Otten, A. Fiore, F. Intonti, R. Sapienza, M. Florescu, M. Gurioli, Near-field investigation of luminescent hyperuniform disordered materials, Adv. Opt. Mater. 10 (8) (2022) 2102565.
[133] S. Aeby, G. Aubry, L. Froufe-Pérez, F. Scheffold, Fabrication of hyperuniform dielectric networks via heat-induced shrinkage reveals a bandgap at telecom wavelengths, Adv. Opt. Mater. 10 (14) (2022) 2200232.
[134] P.M. Piechulla, R.B. Wehrspohn, A.N. Sprafke, Toward hyperuniform disorder via self-assembly of bidisperse colloidal patterns at an electrode, Adv. Mater. Interfaces 10 (3) (2023) 2201395.
[135] J.R. Dale, J.D. Sartor, R.C. Dennis, E.I. Corwin, Hyperuniform jammed sphere packings have anomalous material properties, Phys. Rev. E 106 (2022) 024903.
[136] J. Puig, F. Elías, J. Aragón Sánchez, R. Cortés Maldonado, G. Rumi, G. Nieva, P. Pedrazzini, A.B. Kolton, Y. Fasano, Anisotropic suppression of hyperuniformity of elastic systems in media with planar disorder, Commun. Mater. 3 (1) (2022) 32.
[137] S. Torquato, Extraordinary disordered hyperuniform multifunctional composites, J. Compos. Mater. 56 (23) (2022) 3635–3649.
[138] W. Shi, D. Keeney, D. Chen, Y. Jiao, S. Torquato, Computational design of anisotropic stealthy hyperuniform composites with engineered directional scattering properties, Phys. Rev. E 108 (2023) 045306.
[139] S. Torquato, Structural characterization of many-particle systems on approach to hyperuniform states, Phys. Rev. E 103 (2021) 052126.
[140] H.E. Stanley, Introduction to Phase Transitions and Critical Phenomena, Oxford University Press, New York, 1987.
[141] J.J. Binney, N.J. Dowrick, A.J. Fisher, M.E.J. Newman, The Theory of Critical Phenomena: An Introduction to the Renormalization Group, Oxford University Press, Oxford, England, 1992.
[142] B.B. Mandelbrot, The Fractal Geometry of Nature, W. H. Freeman, New York, 1982.
[143] S. Torquato, J. Kim, M.A. Klatt, Local number fluctuations in hyperuniform and nonhyperuniform systems: Higher-order moments and distribution functions, Phys. Rev. X 11 (2021) 021028.

[144] E.C. Oğuz, J.E.S. Socolar, P.J. Steinhardt, S. Torquato, Hyperuniformity and anti-hyperuniformity in one-dimensional substitution tilings, Acta Cryst. Sect. A: Found. Adv. A 75 (2019) 3–13.
[145] D. Bruggeman, Berechnung verschiedener Physikalischer Konstanten von heterogenen Substanzen, Ann. Phys. (Liepzig) 24 (1935) 636–679.
[146] R. Landauer, The electrical resistance of binary metallic mixtures, J. Appl. Phys. 23 (1952) 779–784.
[147] R. Landauer, Electrical conductivity in inhomogeneous media, in: J.C. Garland, D.B. Tanner (Eds.), Electrical, Transport and Optical Properties of Inhomogeneous Media, AIP, New York, 1978, pp. 2–43.
[148] M. Skolnick, S. Torquato, Accurate formula for the effective conductivity of highly clustered two-phase materials, 2025, arXiv:2503.18715.
[149] M. Beran, Use of the variational approach to determine bounds for the effective permittivity in random media, Nuovo Cimento 38 (1965) 771–782.
[150] G.W. Milton, Bounds on the complex permittivity of a two-component composite material, J. Appl. Phys. 52 (1981) 5286–5293.
[151] Z. Hashin, The elastic moduli of heterogeneous materials, J. Appl. Mech. 29 (1962) 143–150.
[152] F. Murat, L. Tartar, Calcul des variations et homogénéisation, in: Les méthodes d'homogénéisation: Théorie et applications en physique, in: Cours de l'Ecole d'Été d'Analyse Numerique, Eyrolles, Paris, 1985.
[153] K.A. Lurie, A.V. Cherkaev, Exact estimates of the conductivity of a binary mixture of isotropic materials, Proc. R. Soc. Edinb. 104A (1986) 21–38.
[154] G.A. Francfort, F. Murat, Homogenization and optimal bounds in linear elasticity, Arch. Ration. Mech. Anal. 94 (1986) 307–334.
[155] Z. Hashin, B.W. Rosen, The elastic moduli of fiber-reinforced materials, J. Appl. Mech. 31 (1964) 223–232.
[156] A.N. Norris, A differential scheme for the effective moduli of composites, Mech. Mat. 4 (1985) 1–16.
[157] K.A. Lurie, A.V. Cherkaev, The problem of formation of an optimal multicomponent composite, J. Opt. Theor. Appl. 46 (1985) 571–580.
[158] G.W. Milton, Modelling the properties of composites by laminates, in: J.L. Eriksen, et al. (Eds.), Homogenization and Effective Moduli of Materials and Media, Springer-Verlag, New York, 1986.
[159] S. Torquato, G. Stell, Microstructure of two-phase random media: III. The n-point matrix probability functions for fully penetrable spheres, J. Chem. Phys. 79 (1983) 1505–1510.
[160] W. Xia, M.F. Thorpe, Percolation properties of random ellipses, Phys. Rev. A 38 (1988) 2650–2656.
[161] M. Skoge, A. Donev, F.H. Stillinger, S. Torquato, Packing hyperspheres in high-dimensional Euclidean spaces, Phys. Rev. E 74 (2006) 041127.
[162] M.D. Rintoul, S. Torquato, Computer simulations of dense hard-sphere systems, J. Chem. Phys. 105 (1996) 9258–9265, Erratum 107 2698(1997).
[163] F. Lado, S. Torquato, Effective properties of two-phase disordered composite media. I. Simplification of bounds on the conductivity and bulk modulus of dispersions of impenetrable spheres, Phys. Rev. B 33 (1986) 3370–3378.
[164] A.K. Sen, F. Lado, S. Torquato, Bulk properties of composite media: II. Evaluation of bounds on the shear modulus of suspensions of impenetrable spheres, J. Appl. Phys. 62 (1987) 4135–4141.
[165] H.R. Lusti, A.A. Gusev, O. Guseva, The influence of platelet disorientation on the barrier properties of composites: a numerical study, Modelling Simul. Mater. Sci. Eng. 12 (6) (2004) 1201.
[166] A. Norris, The mechanical properties of platelet reinforced composites, Int. J. Solids Struct. 26 (5) (1990) 663–674.
[167] P. Yousefi, H. Malmir, M. Sahimi, Morphology and kinetics of random sequential adsorption of superballs: From hexapods to cubes, Phys. Rev. E 100 (2019) 020602.
[168] S. Torquato, G. Zhang, F.H. Stillinger, Ensemble theory for stealthy hyperuniform disordered ground states, Phys. Rev. X 5 (2015) 021020.
[169] A. Roberts, E. Garboczi, Elastic moduli of model random three-dimensional closed-cell cellular solids, Acta Mater. 49 (2) (2001) 189–197.
[170] R.E. Caflisch, Monte Carlo and quasi-Monte Carlo methods, Acta Numer. 7 (1998) 1–49.
[171] W.H. Press, G.R. Farrar, Recursive stratified sampling for multidimensional Monte Carlo integration, Comput. Phys. 4 (2) (1990) 190–195.
[172] C. Schretter, L. Kobbelt, P.-O. Dehaye, Golden ratio sequences for low-discrepancy sampling, J. Graph. Tools 16 (2012) 95–104.
[173] J.M. Haile, C. Massobrio, S. Torquato, Two-point matrix probability function for two-phase random media: Computer simulation results for impenetrable spheres, J. Chem. Phys. 83 (1985) 4075–4078.
[174] S. Torquato, L.V. Gibiansky, M.J. Silva, L.J. Gibson, Effective mechanical and transport properties of cellular solids, Int. J. Mech. Sci. 40 (1998) 71–82.
[175] R.M. Christensen, Mechanics of cellular and other low density materials, Int. J. Solids Struct. 37 (2000) 93–104.
[176] M. Leuschner, F. Fritzen, Fourier-Accelerated Nodal Solvers (FANS) for homogenization problems, Comput. Mech. 62 (3) (2017).
[177] Y. Jiao, F.H. Stillinger, S. Torquato, A superior descriptor of random textures and its predictive capacity, Proc. Nat. Acad. Sci. 106 (2009) 17634–17639.
[178] S.F.S. Shirazi, S. Gharehkhani, M. Mehrali, H. Yarmand, H.S.C. Metselaar, N.A. Kadri, N.A.A. Osman, A review on powder-based additive manufacturing for tissue engineering: selective laser sintering and inkjet 3d printing, Sci. Tech. Adv. Mater. 16 (2015) 033502.